Journal of the Advanced Program in Plasma Science and Engineering

APPLAuSE

review letters

2019

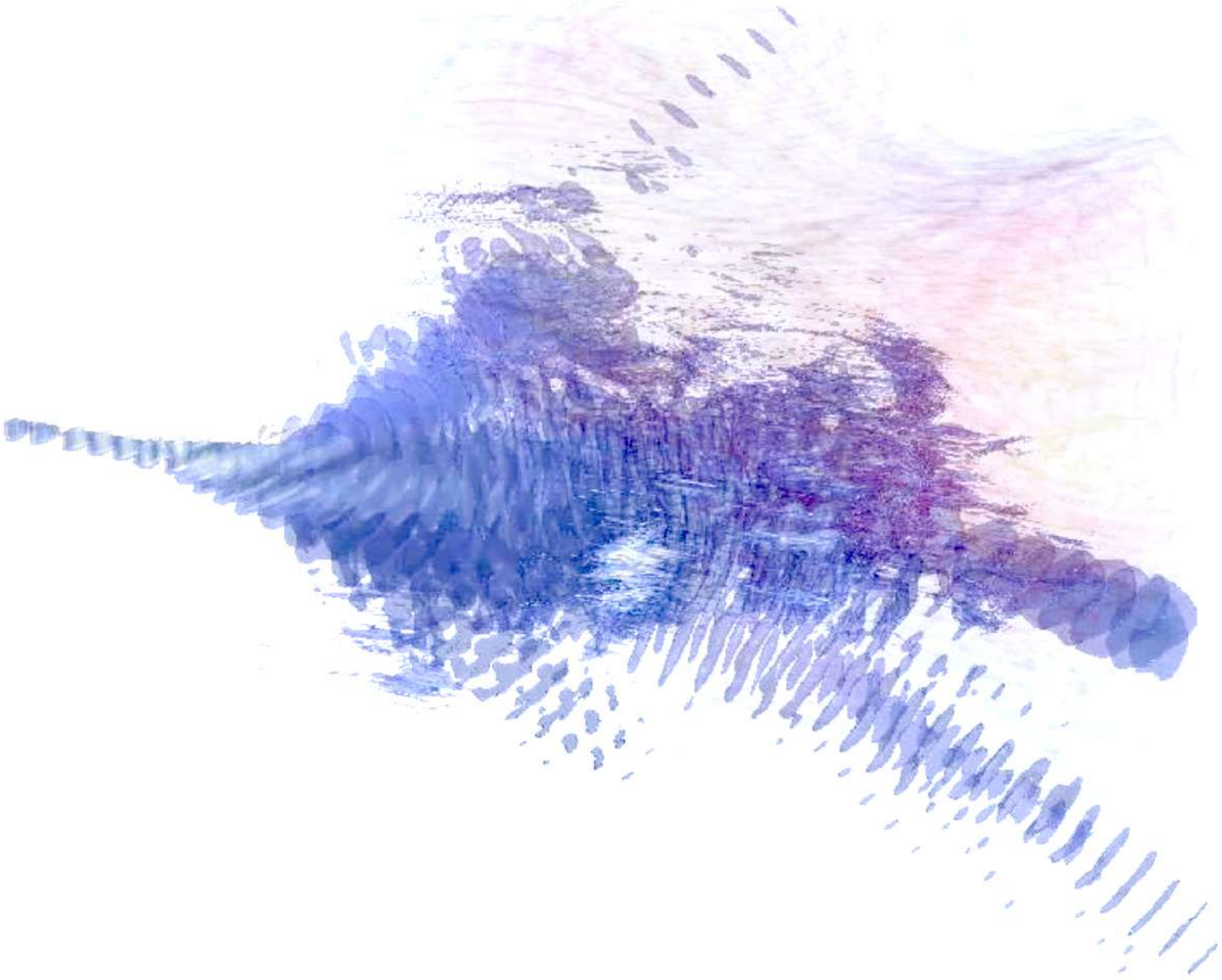

APPLAuSE Review Letters

Organized and Supervised by
Dr. Marta Fajardo

Guest Editor
Ricardo Ferreira

APP. Rev. Let. - February 2019

← Front cover image by Filipe da Silva (IPFN): The electromagnetic field resulting from the interaction between the microwaves emitted by a horn antenna and the plasma. Simulation performed with REFMUL3.

→ Back cover photo - Funding agencies and institutions.

Editor Foreword

It is a pleasure to edit yet another issue of APPLAUSE Review Letters. I would like to personally thank all the members of this year's Soft Skills workshop for the hard work and enthusiasm they revealed while taking part in the course. In particular, I would also like to thank this year's guest editor Ricardo Ferreira for putting together this review, which showcases the work performed by the PhD students from IPFN as they take the first steps in what we hope is a very successful career. Finally, a word of thanks to the anonymous referees from the IPFN, who have been invaluable as usual in their constructive advice.

Marta Fajardo
Instituto de Plasmas e Fusão Nuclear (IPFN), Instituto Superior Técnico
Email: marta.fajardo@tecnico.ulisboa.pt

Guest-editor Foreword

APPLAuSE Review Letters (ARL) is a peer-refereed academic journal on Plasma Physics. The contents of this journal are the collection of the results of APPLAuSE PhD program intensive one week module on Soft Skills. The module helped the students better prepare and write papers for a scientific journal as well as teach them how to review a paper. APPLAuSE Review Letters is composed of reviews and advances made by the students on Plasma Physics.

The fourth issue of ARL was written by APPLAuSE fifth cohort. Each article was reviewed another student and an IPFN senior member. The topics run from plasma astrophysics and planetary exploration to nuclear fusion and plasma jets, from theoretical and numerical approaches to experiments and engineering.

We strived to demonstrate the dedication and maturity of the students and inspire other groups and students to do the same. As a final note I thank to all my colleagues and IPFN senior members who helped review this journal as well as editor and module coordinator Dr. Marta Fajardo.

Ricardo Ferreira
Instituto de Plasmas e Fusão Nuclear (IPFN), Instituto Superior Técnico
Email: ricardojoaogmferreira@tecnico.ulisboa.pt

Contents

Editor Foreword iii

Guest-editor Foreword v

Quasilinear approach to ray-tracing in tokamak plasmas with random density fluctuations 1

Expanding the capabilities of REFMUL3 11

Recent developments on electronics for magnetic diagnostic in nuclear fusion devices 17

Review of Compact Objects Relativistic Magnetospheres 23

Calculation of transport coefficients for fluid modelling of atmospheric pressure plasma jets 29

EAST spectroscopy calibration and experimental results on Mars entry . . . 35

Quasilinear approach to ray-tracing in tokamak plasmas with random density fluctuations

Rui Calado is from Lisbon, Portugal. He obtained both his Bachelor and Master's degree in Engineering Physics at Instituto Superior Técnico in Lisbon. The topic of his Master's Thesis consisted in developing a computational toolkit for plasma physics education. Later he applied to the APPLAuSE PhD Program, in which he is currently enrolled. His research will focus on modelling the losses of energetic ions due to Alfvén modes excited by ICRH in tokamak devices.

Rui Calado

Instituto de Plasmas e Fusão Nuclear (IPFN), Instituto Superior Técnico
Avenida Rovisco Pais, 1049-001 Lisboa, Portugal
E-mail: `rui.p.calado@tecnico.ulisboa.pt`

Abstract. The quasilinear formalism for ray-tracing proposed by Bizarro et al. (2018) is reviewed. This approach allows the tracing of the average ray in a random turbulent media. It is complete in the sense that it provides the full set of equations to trace all the quantities required for the tracing of the ray. Nevertheless, for practical purposes an infinite recurrence needs to be truncated at an appropriate order. The formalism is applied to the example of an ordinary wave propagating in a tokamak plasma.

I. INTRODUCTION

Acquiring information about the plasma in a tokamak is crucial in order to achieve and maintain a safe and efficient operation. Non-intrusive diagnostics are preferred since they avoid perturbing the plasma. Examples of such are magnetic diagnostics [1] and reflectometry techniques [2]. The latter plays an important role in the study of turbulent density fluctuations inside a plasma. It is necessary, however, that the influence of fluctuations on wave propagation is known so that reflectometry measurements may be correctly interpreted [3].

Ray-tracing is one of the most powerful tools to estimate wave propagation in turbulent media. Its application for the study of wave propagation spans over a wide range of scenarios, from sound waves in the ocean [4] to electromagnetic waves in the atmosphere [5]. Several ray-tracing methods and algorithms have been proposed and implemented. In order to study the propagation of waves in turbulent media, ray-tracing techniques usually resort to the simulation of several rays with turbulent profiles differing by a random phase. Afterwards, the mean and root-mean-square of the samples taken is computed.

An alternative method is the statistical, quasilinear approach proposed by Bizarro et al. [6]. This method provides equations for the tracing of average ray properties. Although the tracing of the average ray proves to be more costly than the tracing of a singular ray, it avoids the need for multiple realizations of a ray to obtain the average propagation waves in the medium.

The purpose of this work is to study this novel approach. In Section I the equations of ray-tracing are introduced and the quasilinear formalism is presented. In Section II the formalism is applied to the case of ordinary-waves propagating in tokamak with random density fluctuations. The ordinary mode is the simplest configuration for electromagnetic waves propagating through plasmas subject to a background magnetic field, and as such is a good candidate for a reliable diagnostic in a tokamak.

II. QUASILINEAR FORMALISM FOR RAY-TRACING IN WEAKLY TURBULENT MEDIA

Geometric optics studies the trajectories of rays that represent waves propagating in spatially non-uniform media. The ray equations governing ray trajectory depend on the dispersion relation $D(\omega, \mathbf{r}, \mathbf{k}) = 0$ of the wave being considered. There is no explicit time dependence of D since we will consider scenarios where the transit time of rays across the medium is much less than the characteristic time scale of the fluctuations. From the point of view of such rays, the turbulence is frozen in time. The ray equations take the form

$$\frac{dr_i}{dt} = -\frac{\partial D(\omega, \mathbf{r}, \mathbf{k})/\partial k_i}{\partial D(\omega, \mathbf{r}, \mathbf{k})\partial \omega} \quad \text{and} \quad \frac{dk_i}{dt} = \frac{\partial D(\omega, \mathbf{r}, \mathbf{k})/\partial r_i}{\partial D(\omega, \mathbf{r}, \mathbf{k})\partial \omega}, \tag{1}$$

where $\mathbf{r} = (r_1, r_2, r_3)$ and $\mathbf{k} = (k_1, k_2, k_3)$ are based on a set of generalized coordinates and the respective conjugate momenta and t is a timelike variable related to the propagation along the ray. When one is able to write the dispersion relation in the form

$$D(\omega, \mathbf{r}, \mathbf{k}) = \omega - \Omega(\mathbf{r}, \mathbf{k}) = 0 \tag{2}$$

the ray equations take the Hamiltonian form

$$\frac{dr_i}{dt} = \frac{\partial \Omega(\mathbf{r}, \mathbf{k})}{\partial k_i} \quad \text{and} \quad \frac{dk_i}{dt} = -\frac{\partial \Omega(\mathbf{r}, \mathbf{k})}{\partial r_i}. \tag{3}$$

From 1 we see that $\Omega(\mathbf{r}, \mathbf{k})$ is essentially the wave frequency. Since ω is the most common notation for this wave property, henceforth $\omega(\mathbf{r}, \mathbf{k})$ will be used in the place of $\Omega(\mathbf{r}, \mathbf{k})$.

The statistical approach of the quasilinear method of Bizarro et al. consists in considering the fluctuating quantity, in this case the density, as the sum of a nonfluctuating background plus some random fluctuations, over which the ray equations are then averaged. The rays are also split into ensemble-averaged plus fluctuating terms. We have then

$$n_e(\mathbf{r}) = \langle n_e(\mathbf{r}) \rangle + \delta n_e(\mathbf{r}), \tag{4}$$

$$\mathbf{r} = \langle \mathbf{r} \rangle + \delta \mathbf{r}, \tag{5}$$

$$\mathbf{k} = \langle \mathbf{k} \rangle + \delta \mathbf{k}. \tag{6}$$

Expanding $\omega(\mathbf{r}, \mathbf{k})$ up to second-order in the density fluctuations yields

$$\omega(\mathbf{r}, \mathbf{k}) \simeq \omega_0(\mathbf{r}, \mathbf{k}) + \omega_1(\mathbf{r}, \mathbf{k})\delta n_e(\mathbf{r}) + \omega_2(\mathbf{r}, \mathbf{k})\delta n_e(\mathbf{r})\delta n_e(\mathbf{r}) \tag{7}$$

where

$$\omega_m(\mathbf{r}, \mathbf{k}) \equiv \frac{1}{m!} \left. \frac{\partial^m \omega(\mathbf{r}, \mathbf{k})}{\partial n_e^m} \right|_{\langle n_e(\mathbf{r}) \rangle}. \tag{8}$$

The equations in (3) are then expanded up to second-order in the density and ray fluctuations. Afterwards, the ray equations are ensemble-averaged to yield equations for the propagation of the average ray. These equations are

$$\begin{aligned}\frac{d\langle r_i\rangle}{dt} \simeq & \frac{\partial\omega_0(\langle\mathbf{r}\rangle,\langle\mathbf{k}\rangle)}{\partial k_i} + \frac{1}{2}\frac{\partial^3\omega_0(\langle\mathbf{r}\rangle,\langle\mathbf{k}\rangle)}{\partial k_i\partial r_j\partial r_l}\langle\delta r_j\delta r_l\rangle + \frac{1}{2}\frac{\partial^3\omega_0(\langle\mathbf{r}\rangle,\langle\mathbf{k}\rangle)}{\partial k_i\partial k_j\partial k_l}\langle\delta k_j\delta k_l\rangle + \frac{\partial^3\omega_0(\langle\mathbf{r}\rangle,\langle\mathbf{k}\rangle)}{\partial k_i\partial r_j\partial k_l}\langle\delta r_j\delta k_l\rangle \\ & + \frac{\partial^2\omega_1(\langle\mathbf{r}\rangle,\langle\mathbf{k}\rangle)}{\partial k_i\partial r_j}\langle\delta r_j\delta n_e(\langle\mathbf{r}\rangle)\rangle + \frac{\partial^2\omega_1(\langle\mathbf{r}\rangle,\langle\mathbf{k}\rangle)}{\partial k_i\partial k_j}\langle\delta k_j\delta n_e(\langle\mathbf{r}\rangle)\rangle + \frac{\partial\omega_1(\langle\mathbf{r}\rangle,\langle\mathbf{k}\rangle)}{\partial k_i}\left\langle\delta r_j\frac{\partial\delta n_e(\langle\mathbf{r}\rangle)}{\partial r_j}\right\rangle \\ & + \frac{\partial\omega_2(\langle\mathbf{r}\rangle,\langle\mathbf{k}\rangle)}{\partial k_i}\langle\delta n_e(\langle\mathbf{r}\rangle)\delta n_e(\langle\mathbf{r}\rangle)\rangle,\end{aligned} \tag{9}$$

$$\begin{aligned}\frac{d\langle k_i\rangle}{dt} \simeq & -\frac{\partial\omega_0(\langle\mathbf{r}\rangle,\langle\mathbf{k}\rangle)}{\partial r_i} - \frac{1}{2}\frac{\partial^3\omega_0(\langle\mathbf{r}\rangle,\langle\mathbf{k}\rangle)}{\partial r_i\partial r_j\partial r_l}\langle\delta r_j\delta r_l\rangle - \frac{1}{2}\frac{\partial^3\omega_0(\langle\mathbf{r}\rangle,\langle\mathbf{k}\rangle)}{\partial r_i\partial k_j\partial k_l}\langle\delta k_j\delta k_l\rangle - \frac{\partial^3\omega_0(\langle\mathbf{r}\rangle,\langle\mathbf{k}\rangle)}{\partial r_i\partial r_j\partial k_l}\langle\delta r_j\delta k_l\rangle \\ & - \frac{\partial^2\omega_1(\langle\mathbf{r}\rangle,\langle\mathbf{k}\rangle)}{\partial r_i\partial r_j}\langle\delta r_j\delta n_e(\langle\mathbf{r}\rangle)\rangle - \frac{\partial^2\omega_1(\langle\mathbf{r}\rangle,\langle\mathbf{k}\rangle)}{\partial r_i\partial k_j}\langle\delta k_j\delta n_e(\langle\mathbf{r}\rangle)\rangle - \frac{\partial\omega_1(\langle\mathbf{r}\rangle,\langle\mathbf{k}\rangle)}{\partial r_i}\left\langle\delta r_j\frac{\partial\delta n_e(\langle\mathbf{r}\rangle)}{\partial r_j}\right\rangle \\ & - \frac{\partial\omega_1(\langle\mathbf{r}\rangle,\langle\mathbf{k}\rangle)}{\partial r_j}\left\langle\delta r_j\frac{\partial\delta n_e(\langle\mathbf{r}\rangle)}{\partial r_i}\right\rangle - \frac{\partial\omega_1(\langle\mathbf{r}\rangle,\langle\mathbf{k}\rangle)}{\partial k_j}\left\langle\delta k_j\frac{\partial\delta n_e(\langle\mathbf{r}\rangle)}{\partial r_i}\right\rangle - \omega_1(\langle\mathbf{r}\rangle,\langle\mathbf{k}\rangle)\left\langle\delta r_j\frac{\partial^2\delta n_e(\langle\mathbf{r}\rangle)}{\partial r_j\partial r_i}\right\rangle \\ & - \frac{\partial\omega_2(\langle\mathbf{r}\rangle,\langle\mathbf{k}\rangle)}{\partial r_i}\langle\delta n_e(\langle\mathbf{r}\rangle)\delta n_e(\langle\mathbf{r}\rangle)\rangle - 2\omega_2(\langle\mathbf{r}\rangle,\langle\mathbf{k}\rangle)\left\langle\delta n_e(\langle\mathbf{r}\rangle)\frac{\partial\delta n_e(\langle\mathbf{r}\rangle)}{\partial r_i}\right\rangle.\end{aligned} \tag{10}$$

Only zeroth and second order terms in the fluctuations survive after the averaging process, since we require null average fluctuations, that is $\langle\delta u\rangle \equiv 0$ for any quantity u. In order to trace (9) and (10), equations for the combinations $\langle\delta u_i\delta v_j\rangle$, $\langle\delta u_i\delta n_e(\langle\mathbf{r}\rangle)\rangle$ and $\langle\delta u_i\partial\delta n_e(\langle\mathbf{r}\rangle)/\partial r_j\rangle$, u_i, v_i corresponding to either r_i or k_i, are required. The equations for terms of the form $\langle\delta u_i\delta v_j\rangle$ are computed using the relation

$$\frac{d\langle\delta u\delta v\rangle}{dt} = \left\langle\delta u\frac{d\delta v}{dt}\right\rangle + \left\langle\delta v\frac{d\delta u}{dt}\right\rangle. \tag{11}$$

These equations are then

$$\begin{aligned}\frac{d\langle\delta r_i\delta r_j\rangle}{dt} \simeq & \frac{\partial^2\omega_0(\langle\mathbf{r}\rangle,\langle\mathbf{k}\rangle)}{\partial k_j\partial r_l}\langle\delta r_l\delta r_i\rangle + \frac{\partial^2\omega_0(\langle\mathbf{r}\rangle,\langle\mathbf{k}\rangle)}{\partial k_j\partial k_l}\langle\delta k_l\delta r_i\rangle + \frac{\partial^2\omega_0(\langle\mathbf{r}\rangle,\langle\mathbf{k}\rangle)}{\partial k_i\partial r_l}\langle\delta r_l\delta r_j\rangle + \frac{\partial^2\omega_0(\langle\mathbf{r}\rangle,\langle\mathbf{k}\rangle)}{\partial k_i\partial k_l}\langle\delta k_l\delta r_j\rangle \\ & + \frac{\partial\omega_1(\langle\mathbf{r}\rangle,\langle\mathbf{k}\rangle)}{\partial k_i}\langle\delta r_i\delta n_e(\langle\mathbf{r}\rangle)\rangle + \frac{\partial\omega_1(\langle\mathbf{r}\rangle,\langle\mathbf{k}\rangle)}{\partial k_j}\langle\delta r_j\delta n_e(\langle\mathbf{r}\rangle)\rangle,\end{aligned} \tag{12}$$

$$\begin{aligned}\frac{d\langle\delta k_i\delta k_j\rangle}{dt} \simeq & -\frac{\partial^2\omega_0(\langle\mathbf{r}\rangle,\langle\mathbf{k}\rangle)}{\partial r_j\partial r_l}\langle\delta r_l\delta k_i\rangle - \frac{\partial^2\omega_0(\langle\mathbf{r}\rangle,\langle\mathbf{k}\rangle)}{\partial r_j\partial k_l}\langle\delta k_l\delta k_i\rangle - \frac{\partial^2\omega_0(\langle\mathbf{r}\rangle,\langle\mathbf{k}\rangle)}{\partial r_i\partial r_l}\langle\delta r_l\delta k_j\rangle - \frac{\partial^2\omega_0(\langle\mathbf{r}\rangle,\langle\mathbf{k}\rangle)}{\partial r_i\partial k_l}\langle\delta k_l\delta k_j\rangle \\ & - \frac{\partial\omega_1(\langle\mathbf{r}\rangle,\langle\mathbf{k}\rangle)}{\partial r_j}\langle\delta k_i\delta n_e(\langle\mathbf{r}\rangle)\rangle - \frac{\partial\omega_1(\langle\mathbf{r}\rangle,\langle\mathbf{k}\rangle)}{\partial r_i}\langle\delta k_j\delta n_e(\langle\mathbf{r}\rangle)\rangle - \omega_1(\langle\mathbf{r}\rangle,\langle\mathbf{k}\rangle)\left\langle\delta k_i\frac{\partial\delta n_e(\langle\mathbf{r}\rangle)}{\partial r_j}\right\rangle \\ & - \omega_1(\langle\mathbf{r}\rangle,\langle\mathbf{k}\rangle)\left\langle\delta k_j\frac{\partial\delta n_e(\langle\mathbf{r}\rangle)}{\partial r_i}\right\rangle,\end{aligned} \tag{13}$$

$$\begin{aligned}\frac{d\langle\delta r_i\delta k_j\rangle}{dt} \simeq & -\frac{\partial^2\omega_0(\langle\mathbf{r}\rangle,\langle\mathbf{k}\rangle)}{\partial r_j\partial r_l}\langle\delta r_l\delta r_i\rangle - \frac{\partial^2\omega_0(\langle\mathbf{r}\rangle,\langle\mathbf{k}\rangle)}{\partial r_j\partial k_l}\langle\delta k_l\delta r_i\rangle + \frac{\partial^2\omega_0(\langle\mathbf{r}\rangle,\langle\mathbf{k}\rangle)}{\partial k_i\partial r_l}\langle\delta r_l\delta k_j\rangle + \frac{\partial^2\omega_0(\langle\mathbf{r}\rangle,\langle\mathbf{k}\rangle)}{\partial k_i\partial k_l}\langle\delta k_l\delta k_j\rangle \\ & - \frac{\partial\omega_1(\langle\mathbf{r}\rangle,\langle\mathbf{k}\rangle)}{\partial r_j}\langle\delta r_i\delta n_e(\langle\mathbf{r}\rangle)\rangle + \frac{\partial\omega_1(\langle\mathbf{r}\rangle,\langle\mathbf{k}\rangle)}{\partial k_i}\langle\delta k_j\delta n_e(\langle\mathbf{r}\rangle)\rangle - \omega_1(\langle\mathbf{r}\rangle,\langle\mathbf{k}\rangle)\left\langle\delta r_i\frac{\partial\delta n_e(\langle\mathbf{r}\rangle)}{\partial r_j}\right\rangle.\end{aligned} \tag{14}$$

Finally, we need equations for the terms $\langle\delta u_i\delta f(\langle\mathbf{r}\rangle)\rangle$, where $\delta f(\langle\mathbf{r}\rangle)$ represents $\delta n_e(\langle\mathbf{r}\rangle)$ or any of its derivatives. This is achieved by considering the relation (11) where

$$\frac{d\delta f(\langle\mathbf{r}\rangle)}{dt} = \frac{\partial\delta f(\langle\mathbf{r}\rangle)}{\partial t} + \frac{\partial\delta f(\langle\mathbf{r}\rangle)}{\partial r_i}\frac{d\langle r_i\rangle}{dt}. \tag{15}$$

From the frozen turbulence assumption we neglect the first term of the right-hand side of the equation, to write

$$\frac{d\langle \delta u_i \delta f(\langle \mathbf{r} \rangle)\rangle}{dt} \approx \left\langle \delta u \frac{\partial \delta f(\langle \mathbf{r} \rangle)}{\partial r_i} \right\rangle \frac{d\langle r_i \rangle}{dt} + \left\langle \delta f(\langle \mathbf{r} \rangle) \frac{d\delta u}{dt} \right\rangle . \tag{16}$$

The desired equations computed from the relation (16) can be viewed in APPENDIX A.

III. RAY EQUATIONS FOR THE ORDINARY MODE

Equations (9), (10), (12)-(14) and equations in APPENDIX A constitute the general quasilinear set of ray equations proposed in [6]. So far, no specific wave or background electromagnetic field configuration were assumed. When conceiving reflectometry diagnostics for a tokamak, one has to take into account the effect of the background magnetic field in the propagation of the waves. To illustrate how this is performed, the formalism described in the previous section is applied to the case of the ordinary mode propagating in a tokamak, characterized by the oscillating electric field being aligned with the external magnetic field. As the simplest scenario of electromagnetic waves propagating in a magnetized plasma, it serves as a good example for illustration of the procedure.

The first step is to write the dispersion relation for the ordinary-mode,

$$\omega(\mathbf{r},\mathbf{k}) = \left[\omega_p^2(\mathbf{r}) + k^2c^2\right]^{1/2} = \left[\frac{4\pi e^2}{m_e} n_e(\mathbf{r}) + k^2c^2\right]^{1/2} . \tag{17}$$

When considering the operation of a tokamak, it is convenient to work in toroidal coordinates. Assuming toroidal symmetry, we neglect the toroidal direction ϕ and consider $\mathbf{r} = (\rho, \theta)$ and $\mathbf{k} = (k_\rho, m)$. In this coordinate system, the dispersion relation becomes:

$$\omega(\mathbf{r},\mathbf{k}) = \left[\frac{4\pi e^2}{m_e} n_e(\mathbf{r}) + \left(k_\rho^2 + \frac{m^2}{\rho^2}\right) c^2\right]^{1/2} . \tag{18}$$

Inserting (18) in (8) results in:

$$\omega_0(\langle \mathbf{r} \rangle, \langle \mathbf{k} \rangle) = \left[\frac{4\pi e^2}{m_e} \langle n_e(\langle \mathbf{r} \rangle)\rangle + \left(\langle k_\rho \rangle^2 + \frac{\langle m \rangle^2}{\langle \rho \rangle^2}\right) c^2\right]^{1/2} ; \tag{19}$$

$$\omega_1(\langle \mathbf{r} \rangle, \langle \mathbf{k} \rangle) = \left.\frac{\partial \omega(\mathbf{r},\mathbf{k})}{\partial n_e}\right|_{\langle n_e(\mathbf{r})\rangle, \langle \mathbf{r} \rangle, \langle \mathbf{k} \rangle} = 2\frac{\pi e^2}{m_e} \omega_0^{-1}(\langle \mathbf{r} \rangle, \langle \mathbf{k} \rangle) ; \tag{20}$$

$$\begin{aligned} \omega_2(\langle \mathbf{r} \rangle, \langle \mathbf{k} \rangle) &= \left.\frac{\partial^2 \omega(\mathbf{r},\mathbf{k})}{\partial n_e^2}\right|_{\langle n_e(\mathbf{r})\rangle, \langle \mathbf{r} \rangle, \langle \mathbf{k} \rangle} \\ &= -2\left(\frac{\pi e^2}{m_e}\right)^2 \omega_0^{-3}(\langle \mathbf{r} \rangle, \langle \mathbf{k} \rangle) . \end{aligned} \tag{21}$$

The next step is to compute the derivatives entering in our set of ray equations. An homogeneous background density will be considered for simplification. In the expressions below and until the end of the document, the $\langle\rangle$ was omitted for ρ and wave vector components k_i for the sake of clarity; it is important to keep in mind they are to be considered at their average values, $\langle\rho\rangle$ and $\langle k_i \rangle$. Additionally, ω_0 should be read $\omega_0(\langle \mathbf{r} \rangle, \langle \mathbf{k} \rangle)$. The relevant derivatives take the form:

$$\frac{\partial \omega_0}{\partial \rho} = -\frac{m^2c^2}{\rho^3} \omega_0^{-1} ; \tag{22}$$

$$\frac{\partial \omega_0}{\partial \theta} = 0 ; \tag{23}$$

$$\frac{\partial^2 \omega_0}{\partial \rho \partial \rho} = -\left(\frac{m^4c^4}{\rho^6}\omega_0^{-3} - 3\frac{m^2c^2}{\rho^4}\omega_0^{-1}\right) ; \tag{24}$$

$$\frac{\partial^3 \omega_0}{\partial \rho \partial \rho \partial \rho} = -\left(3\frac{m^6c^6}{\rho^9}\omega_0^{-5} - 9\frac{m^4c^4}{\rho^7}\omega_0^{-3} + 12\frac{m^2c^2}{\rho^5}\omega_0^{-1}\right) ; \tag{25}$$

$$\frac{\partial \omega_0}{\partial k_\rho} = k_\rho c^2 \omega_0^{-1} ; \tag{26}$$

$$\frac{\partial^2 \omega_0}{\partial k_\rho \partial k_\rho} = -\left(k_\rho^2 c^4 \omega_0^{-3} - c^2\omega_0^{-1}\right) ; \tag{27}$$

$$\frac{\partial^3 \omega_0}{\partial k_\rho \partial k_\rho \partial k_\rho} = 3k_\rho^3 c^6 \omega_0^{-5} - 3k_\rho c^4 \omega_0^{-3} ; \tag{28}$$

$$\frac{\partial \omega_0}{\partial m} = \frac{mc^2}{\rho^2} \omega_0^{-1} ; \tag{29}$$

$$\frac{\partial^2 \omega_0}{\partial m \partial m} = -\left(\frac{m^2c^4}{\rho^4}\omega_0^{-3} - \frac{c^2}{\rho^2}\omega_0^{-1}\right) ; \tag{30}$$

$$\frac{\partial^3 \omega_0}{\partial m \partial m \partial m} = 3\frac{m^3c^6}{\rho^6}\omega_0^{-5} - 3\frac{mc^4}{\rho^4}\omega_0^{-3} ; \tag{31}$$

$$\frac{\partial^2\omega_0}{\partial\rho\partial m} = \frac{m^3c^4}{\rho^5}\omega_0^{-3} - 2\frac{mc^2}{\rho^3}\omega_0^{-1}\ ; \tag{32}$$

$$\frac{\partial^3\omega_0}{\partial\rho\partial\rho\partial m} = 3\frac{m^5c^6}{\rho^8}\omega_0^{-5} - 7\frac{m^3c^4}{\rho^6}\omega_0^{-3} + 6\frac{mc^2}{\rho^4}\omega_0^{-1}\ ; \tag{33}$$

$$\frac{\partial^3\omega_0}{\partial\rho\partial m\partial m} = -\left(3\frac{m^4c^6}{\rho^7}\omega_0^{-5} - 5\frac{m^2c^4}{\rho^5}\omega_0^{-3} + 2\frac{c^2}{\rho^3}\omega_0^{-1}\right)\ . \tag{34}$$

The remaining derivatives can be trivially computed using the relations above. The final step is to insert this derivatives in our set of equations. These equations can be found in APPENDIX B.

With the necessary equations derived, the procedure to obtain the average ray propagation is as follows. First, rays are initialized at given coordinates and with a certain conjugate momentum. Then, all quantities in the ray equations are traced along with the ray except for those that depend exclusively on the turbulence profile, which are computed via the introduction of a random phase in the perturbation and subsequent integration to obtain the average effect of random turbulence.

IV. CONCLUSIONS

The quasilinear formalism proposed in [6] as an approach to ray-tracing of waves propagating in weakly turbulent plasmas was reviewed. This formalism is general in terms of density and turbulence profiles and wave configuration. As an example, the formalism was applied to the case of the ordinary mode. The full set of equations that have to be integrated in order to trace both the average ray and its root-mean-square spread were presented for a uniform media with random denisity perturbations and for toroidal coordinates and the corresponding canonically conjugate wave vectors. This approach is fully developed and it may be numerically implemented provided that the dispersion relation is written in the shape shown in (2) and the infinite recurrence in APPENDIX A is truncated.

APPENDIX A

The equations for the terms $\langle \delta u_i \delta f(\langle \mathbf{r} \rangle)\rangle$, where $\delta f(\langle \mathbf{r}\rangle)$ represents $\delta n_e(\langle \mathbf{r}\rangle)$ or any of its derivatives are

$$\begin{aligned}\frac{d\langle \delta r_i \delta n_e(\langle \mathbf{r}\rangle)\rangle}{dt} \simeq& \left\langle \delta r_i \frac{\partial \delta n_e(\langle \mathbf{r}\rangle)}{\partial r_j}\right\rangle \frac{d\langle r_j\rangle}{dt} + \frac{\partial^2\omega_0(\langle \mathbf{r}\rangle,\langle \mathbf{k}\rangle)}{\partial k_i \partial r_j}\langle \delta r_j \delta n_e(\langle \mathbf{r}\rangle)\rangle + \frac{\partial^2\omega_0(\langle \mathbf{r}\rangle,\langle \mathbf{k}\rangle)}{\partial k_i \partial k_j}\langle \delta k_j \delta n_e(\langle \mathbf{r}\rangle)\rangle \\ &+ \frac{\partial \omega_1(\langle \mathbf{r}\rangle,\langle \mathbf{k}\rangle)}{\partial k_i}\langle \delta n_e(\langle \mathbf{r}\rangle)\delta n_e(\langle \mathbf{r}\rangle)\rangle,\end{aligned} \tag{35}$$

$$\begin{aligned}\frac{d\langle \delta k_i \delta n_e(\langle \mathbf{r}\rangle)\rangle}{dt} \simeq& \left\langle \delta k_i \frac{\partial \delta n_e(\langle \mathbf{r}\rangle)}{\partial r_j}\right\rangle \frac{d\langle r_j\rangle}{dt} - \frac{\partial^2\omega_0(\langle \mathbf{r}\rangle,\langle \mathbf{k}\rangle)}{\partial r_i \partial r_j}\langle \delta r_j \delta n_e(\langle \mathbf{r}\rangle)\rangle - \frac{\partial^2\omega_0(\langle \mathbf{r}\rangle,\langle \mathbf{k}\rangle)}{\partial r_i \partial k_j}\langle \delta k_j \delta n_e(\langle \mathbf{r}\rangle)\rangle \\ &- \frac{\partial \omega_1(\langle \mathbf{r}\rangle,\langle \mathbf{k}\rangle)}{\partial r_i}\langle \delta n_e(\langle \mathbf{r}\rangle)\delta n_e(\langle \mathbf{r}\rangle)\rangle - \omega_1(\langle \mathbf{r}\rangle,\langle \mathbf{k}\rangle)\left\langle \delta n_e(\langle \mathbf{r}\rangle)\frac{\partial \delta n_e(\langle \mathbf{r}\rangle)}{\partial r_i}\right\rangle,\end{aligned} \tag{36}$$

$$\begin{aligned}\frac{d}{dt}\left\langle \delta r_i \frac{\partial \delta n_e(\langle \mathbf{r}\rangle)}{\partial r_j}\right\rangle \simeq& \left\langle \delta r_i \frac{\partial^2 \delta n_e(\langle \mathbf{r}\rangle)}{\partial r_j \partial r_l}\right\rangle \frac{d\langle \mathbf{r_l}\rangle}{dt} + \frac{\partial^2\omega_0(\langle \mathbf{r}\rangle,\langle \mathbf{k}\rangle)}{\partial k_i \partial r_l}\left\langle \delta r_l \frac{\partial \delta n_e(\langle \mathbf{r}\rangle)}{\partial r_j}\right\rangle + \frac{\partial^2\omega_0(\langle \mathbf{r}\rangle,\langle \mathbf{k}\rangle)}{\partial k_i \partial k_l}\left\langle \delta k_l \frac{\partial \delta n_e(\langle \mathbf{r}\rangle)}{\partial r_j}\right\rangle \\ &+ \frac{\partial \omega_1(\langle \mathbf{r}\rangle,\langle \mathbf{k}\rangle)}{\partial k_i}\left\langle \delta n_e(\langle \mathbf{r}\rangle)\frac{\partial \delta n_e(\langle \mathbf{r}\rangle)}{\partial r_j}\right\rangle,\end{aligned} \tag{37}$$

$$\begin{aligned}\frac{d}{dt}\left\langle \delta k_i \frac{\partial \delta n_e(\langle \mathbf{r}\rangle)}{\partial r_j}\right\rangle \simeq& \left\langle \delta k_i \frac{\partial^2 \delta n_e(\langle \mathbf{r}\rangle)}{\partial r_j \partial r_l}\right\rangle \frac{d\langle \mathbf{r_l}\rangle}{dt} - \frac{\partial^2\omega_0(\langle \mathbf{r}\rangle,\langle \mathbf{k}\rangle)}{\partial r_i \partial r_l}\left\langle \delta r_l \frac{\partial \delta n_e(\langle \mathbf{r}\rangle)}{\partial r_j}\right\rangle - \frac{\partial^2\omega_0(\langle \mathbf{r}\rangle,\langle \mathbf{k}\rangle)}{\partial r_i \partial k_l}\left\langle \delta k_l \frac{\partial \delta n_e(\langle \mathbf{r}\rangle)}{\partial r_j}\right\rangle \\ &- \frac{\partial \omega_1(\langle \mathbf{r}\rangle,\langle \mathbf{k}\rangle)}{\partial r_i}\left\langle \delta n_e(\langle \mathbf{r}\rangle)\frac{\partial \delta n_e(\langle \mathbf{r}\rangle)}{\partial r_j}\right\rangle - \omega_1(\langle \mathbf{r}\rangle,\langle \mathbf{k}\rangle)\left\langle \frac{\partial \delta n_e(\langle \mathbf{r}\rangle)}{\partial r_i}\frac{\partial \delta n_e(\langle \mathbf{r}\rangle)}{\partial r_j}\right\rangle.\end{aligned} \tag{38}$$

It is important to note that the system is closed by a downward infinite recurrence, in the sense that to trace terms containing a derivative of order m of the perturbation on the density it is required that the derivative of order $m+1$ is known. The expression defining this recurrence is written below

$$\frac{d}{dt}\left\langle \delta u \frac{\partial^m \delta n_e(\langle \mathbf{r}\rangle)}{\partial r_{i_1}\partial r_{i_2}...\partial r_{i_m}}\right\rangle \simeq \left\langle \delta u \frac{\partial^{m+1} \delta n_e(\langle \mathbf{r}\rangle)}{\partial r_{i_1}\partial r_{i_2}...\partial r_{i_m}\partial r_{i_{m+1}}}\right\rangle \frac{d\langle r_{i_{m+1}}\rangle}{dt} + \left\langle \frac{\partial^m \delta n_e(\langle \mathbf{r}\rangle)}{\partial r_{i_1}\partial r_{i_2}...\partial r_{i_m}}\frac{d\delta u}{dt}\right\rangle. \tag{39}$$

When applied to a numerical ray-tracing method, this recurrence needs to be truncated at some order m by

ignoring in (39) the first term in the right-hand side.

APPENDIX B

The quasilinear ray equations for the ordinary mode are:

$$\begin{aligned}
\frac{d\langle\rho\rangle}{dt} \simeq\ & k_\rho c^2\omega_0^{-1} + \frac{1}{2}\left(3\frac{k_\rho m^4c^6}{\rho^6}\omega_0^{-5} - 3\frac{k_\rho m^2c^4}{\rho^4}\omega_0^{-3}\right)\langle\delta\rho\delta\rho\rangle + \frac{1}{2}\left(3k_\rho^3c^6\omega_0^{-5} - 3k_\rho c^4\omega_0^{-3}\right)\langle\delta k_\rho\delta k_\rho\rangle \\
& + \left(3\frac{k_\rho^2 mc^6}{\rho^2}\omega_0^{-5} - \frac{mc^4}{\rho^2}\omega_0^{-3}\right)\langle\delta k_\rho\delta m\rangle + \frac{1}{2}\left(3\frac{k_\rho m^2c^6}{\rho^4}\omega_0^{-5} - \frac{k_\rho c^4}{\rho^2}\omega_0^{-3}\right)\langle\delta m\delta m\rangle \\
& + \left(\frac{m^2c^4}{\rho^3}\omega_0^{-3} - 3\frac{k_\rho^2m^2c^6}{\rho^3}\omega_0^{-5}\right)\langle\delta\rho\delta k_\rho\rangle + \left(2\frac{k_\rho mc^4}{\rho^3}\omega_0^{-3} - 3\frac{k_\rho m^3c^6}{\rho^5}\omega_0^{-5}\right)\langle\delta\rho\delta m\rangle \\
& - 6\frac{\pi e^2}{m_e}\frac{k_\rho m^2c^4}{\rho^3}\omega_0^{-5}\langle\delta\rho\delta n_e(\langle\mathbf{r}\rangle)\rangle + \left(6\frac{\pi e^2}{m_e}k_\rho^2c^4\omega_0^{-5} - 2\frac{\pi e^2}{me}c^2\omega_0^{-3}\right)\langle\delta k_\rho\delta n_e(\langle\mathbf{r}\rangle)\rangle \\
& + 6\frac{\pi e^2}{m_e}\frac{k_\rho mc^4}{\rho^2}\omega_0^{-5}\langle\delta m\delta n_e(\langle\mathbf{r}\rangle)\rangle - 2\frac{\pi e^2}{m_e}k_\rho c^2\omega_0^{-3}\left\langle\delta\rho\frac{\partial\delta n_e(\langle\mathbf{r}\rangle)}{\partial\rho}\right\rangle - 2\frac{\pi e^2}{m_e}k_\rho c^2\omega_0^{-3}\left\langle\delta\theta\frac{\partial\delta n_e(\langle\mathbf{r}\rangle)}{\partial\theta}\right\rangle \\
& + 6\left(\frac{\pi e^2}{m_e}\right)^2 k_\rho c^2\omega_0^{-5}\langle\delta n_e(\langle\mathbf{r}\rangle)\delta n_e(\langle\mathbf{r}\rangle)\rangle\ ; \qquad (40)
\end{aligned}$$

$$\begin{aligned}
\frac{d\langle\theta\rangle}{dt} \simeq\ & \frac{mc^2}{\rho^2}\omega_0^{-1} + \frac{1}{2}\left(3\frac{m^5c^6}{\rho^8}\omega_0^{-5} - 7\frac{m^3c^4}{\rho^6}\omega_0^{-3} + 6\frac{mc^2}{\rho^4}\omega_0^{-1}\right)\langle\delta\rho\delta\rho\rangle \\
& + \frac{1}{2}\left(3\frac{k_\rho^2mc^6}{\rho^2}\omega_0^{-5} - \frac{mc^4}{\rho^2}\omega_0^{-3}\right)\langle\delta k_\rho\delta k_\rho\rangle + \frac{1}{2}\left(3\frac{m^3c^6}{\rho^6}\omega_0^{-5} - 3\frac{mc^4}{\rho^4}\omega_0^{-3}\right)\langle\delta m\delta m\rangle \\
& + \left(3\frac{k_\rho m^2c^6}{\rho^4}\omega_0^{-5} - \frac{k_\rho c^4}{\rho^2}\omega_0^{-3}\right)\langle\delta k_\rho\delta m\rangle - \left(3\frac{k_\rho m^3c^6}{\rho^5}\omega_0^{-5} - 2\frac{k_\rho mc^4}{\rho^3}\omega_0^{-3}\right)\langle\delta\rho\delta k_\rho\rangle\,; \\
& - \left(3\frac{m^4c^6}{\rho^7}\omega_0^{-5} - 5\frac{m^2c^4}{\rho^5}\omega_0^{-3} + 2\frac{c^2}{\rho^3}\omega_0^{-1}\right)\langle\delta\rho\delta m\rangle - 2\frac{\pi e^2}{m_e}\left(3\frac{m^3c^4}{\rho^5}\omega_0^{-5} - 2\frac{mc^2}{\rho^3}\omega_0^{-3}\right)\langle\delta\rho\delta n_e(\langle\mathbf{r}\rangle)\rangle \\
& + 6\frac{\pi e^2}{m_e}\frac{k_\rho mc^4}{\rho^2}\omega_0^{-5}\langle\delta k_\rho\delta n_e(\langle\mathbf{r}\rangle)\rangle + 2\frac{\pi e^2}{m_e}\left(3\frac{m^2c^4}{\rho^4}\omega_0^{-5} - \frac{c^2}{\rho^2}\omega_0^{-3}\right)\langle\delta m\delta n_e(\langle\mathbf{r}\rangle)\rangle \\
& - 2\frac{\pi e^2}{m_e}\frac{mc^2}{\rho^2}\omega_0^{-3}\left\langle\delta\rho\frac{\partial\delta n_e(\langle\mathbf{r}\rangle)}{\partial\rho}\right\rangle - 2\frac{\pi e^2}{m_e}\frac{mc^2}{\rho^2}\omega_0^{-3}\left\langle\delta\theta\frac{\partial\delta n_e(\langle\mathbf{r}\rangle)}{\partial\theta}\right\rangle + 6\left(\frac{\pi e^2}{m_e}\right)^2\frac{mc^2}{\rho^2}\omega_0^{-5}\langle\delta n_e(\langle\mathbf{r}\rangle)\delta n_e(\langle\mathbf{r}\rangle)\rangle\ ; \qquad (41)
\end{aligned}$$

$$\frac{d\langle\delta\rho\delta\rho\rangle}{dt} \simeq 2\frac{k_\rho m^2c^4}{\rho^3}\omega_0^{-3}\langle\delta\rho\delta\rho\rangle - 2\left(k_\rho^2c^4\omega_0^{-3} - c^2\omega_0^{-1}\right)\langle\delta k_\rho\delta\rho\rangle - 2\frac{k_\rho mc^4}{\rho^2}\omega_0^{-3}\langle\delta m\delta\rho\rangle - 4\frac{\pi e^2}{m_e}k_\rho c^2\omega_0^{-3}\langle\delta\rho\delta n_e(\langle\mathbf{r}\rangle)\rangle\ ; \qquad (42)$$

$$\begin{aligned}
\frac{d\langle\delta\theta\delta\theta\rangle}{dt} \simeq\ & 2\left(\frac{m^3c^4}{\rho^5}\omega_0^{-3} - 2\frac{mc^2}{\rho^3}\omega_0^{-1}\right)\langle\delta\rho\delta\theta\rangle - 2\left(\frac{m^2c^4}{\rho^4}\omega_0^{-3} - \frac{c^2}{\rho^2}\omega_0^{-1}\right)\langle\delta m\delta\theta\rangle - 2\frac{k_\rho mc^4}{\rho^2}\omega_0^{-3}\langle\delta k_\rho\delta\theta\rangle \\
& - 4\frac{\pi e^2}{m_e}\frac{mc^2}{\rho^2}\omega_0^{-3}\langle\delta\theta\delta n_e(\langle\mathbf{r}\rangle)\rangle\ ; \qquad (43)
\end{aligned}$$

$$\frac{d\langle\delta\rho\delta\theta\rangle}{dt} \simeq \left(\frac{m^3c^4}{\rho^5}\omega_0^{-3} - 2\frac{mc^2}{\rho^3}\omega_0^{-1}\right)\langle\delta\rho\delta\rho\rangle - \frac{k_\rho mc^4}{\rho^2}\omega_0^{-3}\langle\delta k_\rho\delta\rho\rangle - \left(\frac{m^2c^4}{\rho^4}\omega_0^{-3} - \frac{c^2}{\rho^2}\omega_0^{-1}\right)\langle\delta m\delta\rho\rangle + \frac{k_\rho m^2c^4}{\rho^3}\omega_0^{-3}\langle\delta\rho\delta\theta\rangle \tag{44}$$

$$- \left(k_\rho^2c^4\omega_0^{-3} - c^2\omega_0^{-1}\right)\langle\delta k_\rho\delta\theta\rangle - \frac{k_\rho mc^4}{\rho^2}\omega_0^{-3}\langle\delta m\delta\theta\rangle - 2\frac{\pi e^2}{m_e}\frac{mc^2}{\rho^2}\omega_0^{-3}\langle\delta\rho\delta n_e(\langle\mathbf{r}\rangle)\rangle - 2\frac{\pi e^2}{m_e}k_\rho c^2\omega_0^{-3}\langle\delta\theta\delta n_e(\langle\mathbf{r}\rangle)\rangle \tag{45}$$

$$\begin{aligned}\frac{d\langle k_\rho\rangle}{dt} \simeq\ & \frac{m^2c^2}{\rho^3}\omega_0^{-1} + \frac{1}{2}\left(3\frac{m^6c^6}{\rho^9}\omega_0^{-5} - 9\frac{m^4c^4}{\rho^7}\omega_0^{-3} + 12\frac{m^2c^2}{\rho^5}\omega_0^{-1}\right)\langle\delta\rho\delta\rho\rangle \\ & + \frac{1}{2}\left(3\frac{k_\rho^2m^2c^6}{\rho^3}\omega_0^{-5} - \frac{m^2c^4}{\rho^3}\omega_0^{-3}\right)\langle\delta k_\rho\delta k_\rho\rangle + \frac{1}{2}\left(3\frac{m^4c^6}{\rho^7}\omega_0^{-5} - 5\frac{m^2c^4}{\rho^5}\omega_0^{-3} + 2\frac{c^2}{\rho^3}\omega_0^{-1}\right)\langle\delta m\delta m\rangle \\ & + \left(3\frac{k_\rho m^3c^6}{\rho^5}\omega_0^{-5} - 2\frac{k_\rho mc^4}{\rho^3}\omega_0^{-3}\right)\langle\delta k_\rho\delta m\rangle - \left(3\frac{k_\rho m^4c^6}{\rho^6}\omega_0^{-5} - 3\frac{k_\rho m^2c^4}{\rho^4}\omega_0^{-3}\right)\langle\delta\rho\delta k_\rho\rangle \\ & - \left(3\frac{m^5c^6}{\rho^8}\omega_0^{-5} - 7\frac{m^3c^4}{\rho^6}\omega_0^{-3} + 6\frac{mc^2}{\rho^4}\omega_0^{-1}\right)\langle\delta\rho\delta m\rangle - 2\frac{\pi e^2}{m_e}\left(3\frac{m^4c^4}{\rho^6}\omega_0^{-5} - 3\frac{m^2c^2}{\rho^4}\omega_0^{-3}\right)\langle\delta\rho\delta n_e(\langle\mathbf{r}\rangle)\rangle \\ & + 6\frac{\pi e^2}{m_e}\frac{k_\rho m^2c^4}{\rho^3}\omega_0^{-5}\langle\delta k_\rho\delta n_e(\langle\mathbf{r}\rangle)\rangle + 2\frac{\pi e^2}{m_e}\left(3\frac{m^3c^4}{\rho^5}\omega_0^{-5} - 2\frac{mc^2}{\rho^3}\omega_0^{-3}\right)\langle\delta m\delta n_e(\langle\mathbf{r}\rangle)\rangle \\ & - 4\frac{\pi e^2}{m_e}\frac{m^2c^2}{\rho^3}\omega_0^{-3}\left\langle\delta\rho\frac{\partial\delta n_e(\langle\mathbf{r}\rangle)}{\partial\rho}\right\rangle - 2\frac{\pi e^2}{m_e}\frac{m^2c^2}{\rho^3}\omega_0^{-3}\left\langle\delta\theta\frac{\partial\delta n_e(\langle\mathbf{r}\rangle)}{\partial\theta}\right\rangle + 2\frac{\pi e^2}{m_e}k_\rho c^2\omega_0^{-3}\left\langle\delta k_\rho\frac{\partial\delta n_e(\langle\mathbf{r}\rangle)}{\partial\rho}\right\rangle \\ & + 2\frac{\pi e^2}{m_e}\frac{mc^2}{\rho^2}\omega_0^{-3}\left\langle\delta m\frac{\partial\delta n_e(\langle\mathbf{r}\rangle)}{\partial\rho}\right\rangle - 2\frac{\pi e^2}{m_e}\omega_0^{-1}\left\langle\delta\rho\frac{\partial^2\delta n_e(\langle\mathbf{r}\rangle)}{\partial\rho\partial\rho}\right\rangle - 2\frac{\pi e^2}{m_e}\omega_0^{-1}\left\langle\delta\theta\frac{\partial^2\delta n_e(\langle\mathbf{r}\rangle)}{\partial\rho\partial\theta}\right\rangle \\ & + 6\left(\frac{\pi e^2}{m_e}\right)^2\frac{m^2c^2}{\rho^3}\omega_0^{-5}\langle\delta n_e(\langle\mathbf{r}\rangle)\delta n_e(\langle\mathbf{r}\rangle)\rangle + 4\left(\frac{\pi e^2}{m_e}\right)^2\omega_0^{-3}\left\langle\delta n_e(\langle\mathbf{r}\rangle)\frac{\partial\delta n_e(\langle\mathbf{r}\rangle)}{\partial\rho}\right\rangle\ ; \end{aligned} \tag{46}$$

$$\begin{aligned}\frac{d\langle m\rangle}{dt} \simeq\ & - 2\frac{\pi e^2}{m_e}\frac{m^2c^2}{\rho^3}\omega_0^{-3}\left\langle\delta\rho\frac{\partial\delta n_e(\langle\mathbf{r}\rangle)}{\partial\theta}\right\rangle + 2\frac{\pi e^2}{m_e}k_\rho c^2\omega_0^{-3}\left\langle\delta k_\rho\frac{\partial\delta n_e(\langle\mathbf{r}\rangle)}{\partial\theta}\right\rangle \\ & + 2\frac{\pi e^2}{m_e}\frac{mc^2}{\rho^2}\omega_0^{-3}\left\langle\delta m\frac{\partial\delta n_e(\langle\mathbf{r}\rangle)}{\partial\theta}\right\rangle - 2\frac{\pi e^2}{m_e}\omega_0^{-1}\left\langle\delta\rho\frac{\partial^2\delta n_e(\langle\mathbf{r}\rangle)}{\partial\rho\partial\theta}\right\rangle - 2\frac{\pi e^2}{m_e}\omega_0^{-1}\left\langle\delta\theta\frac{\partial^2\delta n_e(\langle\mathbf{r}\rangle)}{\partial\theta\partial\theta}\right\rangle \\ & + 4\left(\frac{\pi e^2}{m_e}\right)^2\omega_0^{-3}\left\langle\delta n_e(\langle\mathbf{r}\rangle)\frac{\partial\delta n_e(\langle\mathbf{r}\rangle)}{\partial\theta}\right\rangle\ ; \end{aligned} \tag{47}$$

$$\begin{aligned}\frac{d\langle\delta k_\rho\delta k_\rho\rangle}{dt} \simeq\ & 2\left(\frac{m^4c^4}{\rho^6}\omega_0^{-3} - 3\frac{m^2c^2}{\rho^4}\omega_0^{-1}\right)\langle\delta\rho\delta k_\rho\rangle - 2\frac{k_\rho m^2c^4}{\rho^3}\omega_0^{-3}\langle\delta k_\rho\delta k_\rho\rangle - 2\left(\frac{m^3c^4}{\rho^5}\omega_0^{-3} - 2\frac{mc^2}{\rho^3}\omega_0^{-1}\right)\langle\delta m\delta k_\rho\rangle \\ & - 4\frac{\pi e^2}{m_e}\frac{m^2c^2}{\rho^3}\omega_0^{-3}\langle\delta k_\rho\delta n_e(\langle\mathbf{r}\rangle)\rangle - 4\frac{\pi e^2}{m_e}\omega_0^{-1}\left\langle\delta k_\rho\frac{\partial\delta n_e(\langle\mathbf{r}\rangle)}{\partial\rho}\right\rangle\ ; \end{aligned} \tag{48}$$

$$\frac{d\langle\delta m\delta m\rangle}{dt} \simeq - 4\frac{\pi e^2}{m_e}\omega_0^{-1}\left\langle\delta m\frac{\partial\delta n_e(\langle\mathbf{r}\rangle)}{\partial\theta}\right\rangle \tag{49}$$

$$\begin{aligned}\frac{d\langle\delta k_\rho\delta m\rangle}{dt} \simeq\ & \left(\frac{m^4c^4}{\rho^6}\omega_0^{-3} - 3\frac{m^2c^2}{\rho^4}\omega_0^{-1}\right)\langle\delta\rho\delta m\rangle - \frac{k_\rho m^2c^4}{\rho^3}\omega_0^{-3}\langle\delta k_\rho\delta m\rangle - \left(\frac{m^3c^4}{\rho^5}\omega_0^{-3} + 2\frac{mc^2}{\rho^3}\omega_0^{-1}\right)\langle\delta m\delta m\rangle \\ & - 2\frac{\pi e^2}{m_e}\frac{m^2c^2}{\rho^3}\omega_0^{-3}\langle\delta m\delta n_e(\langle\mathbf{r}\rangle)\rangle - 2\frac{\pi e^2}{m_e}\omega_0^{-1}\left\langle\delta k_\rho\frac{\partial\delta n_e(\langle\mathbf{r}\rangle)}{\partial\theta}\right\rangle - 2\frac{\pi e^2}{m_e}\omega_0^{-1}\left\langle\delta m\frac{\partial\delta n_e(\langle\mathbf{r}\rangle)}{\partial\rho}\right\rangle\ ; \end{aligned} \tag{50}$$

$$\frac{d\langle\delta\rho\delta k_\rho\rangle}{dt} \simeq \left(\frac{m^4c^4}{\rho^6}\omega_0^{-3} - 3\frac{m^2c^2}{\rho^4}\omega_0^{-1}\right)\langle\delta\rho\delta\rho\rangle - \left(\frac{m^3c^4}{\rho^5}\omega_0^{-3} - 2\frac{mc^2}{\rho^3}\omega_0^{-1}\right)\langle\delta m\delta\rho\rangle \tag{51}$$

$$- \left(k_\rho^2c^4\omega_0^{-3} + c^2\omega_0^{-1}\right)\langle\delta k_\rho\delta k_\rho\rangle - \frac{k_\rho mc^4}{\rho^2}\omega_0^{-3}\langle\delta m\delta k_\rho\rangle - 2\frac{\pi e^2}{m_e}\frac{m^2c^2}{\rho^3}\omega_0^{-3}\langle\delta\rho\delta n_e(\langle\mathbf{r}\rangle)\rangle$$

$$- 2\frac{\pi e^2}{m_e}k_\rho c^2\omega_0^{-3}\langle k_\rho\delta n_e(\langle\mathbf{r}\rangle)\rangle - 2\frac{\pi e^2}{m_e}\omega_0^{-1}\left\langle\delta\rho\frac{\partial\delta n_e(\langle\mathbf{r}\rangle)}{\partial\rho}\right\rangle \ ; \tag{52}$$

$$\frac{d\langle\delta\rho\delta m\rangle}{dt} \simeq \frac{k_\rho m^2c^4}{\rho^3}\omega_0^{-3}\langle\delta\rho\delta m\rangle - \left(k_\rho^2c^4\omega_0^{-3} - c^2\omega_0^{-1}\right)\langle\delta k_\rho\delta m\rangle - \frac{k_\rho mc^4}{\rho^2}\omega_0^{-3}\langle\delta m\delta m\rangle$$

$$- 2\frac{\pi e^2}{m_e}k_\rho c^2\omega_0^{-3}\langle\delta m\delta n_e(\langle\mathbf{r}\rangle)\rangle - 2\frac{\pi e^2}{m_e}\omega_0^{-1}\left\langle\delta\rho\frac{\partial\delta n_e(\langle\mathbf{r}\rangle)}{\partial\theta}\right\rangle \ ; \tag{53}$$

$$\frac{d\langle\delta\theta\delta k_\rho\rangle}{dt} \simeq \left(\frac{m^4c^4}{\rho^6}\omega_0^{-3} - 3\frac{m^2c^2}{\rho^4}\omega_0^{-1}\right)\langle\delta\rho\delta\theta\rangle - \frac{k_\rho m^2c^4}{\rho^3}\omega_0^{-3}\langle\delta k_\rho\delta\theta\rangle$$

$$- \left(\frac{m^3c^4}{\rho^5}\omega_0^{-3} - 2\frac{mc^2}{\rho^3}\omega_0^{-1}\right)\langle\delta m\delta\theta\rangle + \left(\frac{m^3c^4}{\rho^5}\omega_0^{-3} - 2\frac{mc^2}{\rho^3}\omega_0^{-1}\right)\langle\delta\rho\delta k_\rho\rangle - \frac{k_\rho mc^4}{\rho^2}\omega_0^{-3}\langle\delta k_\rho\delta k_\rho\rangle$$

$$- \left(\frac{m^2c^4}{\rho^4}\omega_0^{-3} - \frac{c^2}{\rho^2}\omega_0^{-1}\right)\langle\delta m\delta k_\rho\rangle - 2\frac{\pi e^2}{m_e}\frac{m^2c^2}{\rho^3}\omega_0^{-3}\langle\delta\theta\delta n_e(\langle\mathbf{r}\rangle)\rangle$$

$$- 2\frac{\pi e^2}{m_e}\frac{mc^2}{\rho^2}\omega_0^{-3}\langle\delta k_\rho\delta n_e(\langle\mathbf{r}\rangle)\rangle - 2\frac{\pi e^2}{m_e}\omega_0^{-1}\left\langle\delta\theta\frac{\partial\delta n_e(\langle\mathbf{r}\rangle)}{\partial\rho}\right\rangle \ ; \tag{54}$$

$$\frac{d\langle\delta\theta\delta m\rangle}{dt} \simeq \left(\frac{m^3c^4}{\rho^5}\omega_0^{-3} - 2\frac{mc^2}{\rho^3}\omega_0^{-1}\right)\langle\delta\rho\delta m\rangle - \frac{k_\rho mc^4}{\rho^2}\omega_0^{-3}\langle\delta k_\rho\delta m\rangle - \left(\frac{m^2c^4}{\rho^4}\omega_0^{-3} - \frac{c^2}{\rho^2}\omega_0^{-1}\right)\langle\delta m\delta m\rangle$$

$$- 2\frac{\pi e^2}{m_e}\frac{mc^2}{\rho^2}\omega_0^{-3}\langle\delta m\delta n_e(\langle\mathbf{r}\rangle)\rangle - 2\frac{\pi e^2}{m_e}\omega_0^{-1}\left\langle\delta\theta\frac{\partial\delta n_e(\langle\mathbf{r}\rangle)}{\partial\theta}\right\rangle \ ; \tag{55}$$

$$\frac{d\langle\delta\rho\delta n_e(\langle\mathbf{r}\rangle)}{dt} \simeq \left\langle\delta\rho\frac{\partial\delta n_e(\langle\mathbf{r}\rangle)}{\partial\rho}\right\rangle\frac{d\langle\rho\rangle}{dt} + \left\langle\delta\rho\frac{\partial\delta n_e(\langle\mathbf{r}\rangle)}{\partial\theta}\right\rangle\frac{d\langle\theta\rangle}{dt} + \frac{k_\rho m^2c^4}{\rho^3}\omega_0^{-3}\langle\delta\rho\delta n_e(\langle\mathbf{r}\rangle)\rangle$$

$$- \left(k_\rho^2c^4\omega_0^{-3} - c^2\omega_0^{-1}\right)\langle\delta k_\rho\delta n_e(\langle\mathbf{r}\rangle)\rangle - \frac{k_\rho mc^4}{\rho^2}\omega_0^{-3}\langle\delta m\delta n_e(\langle\mathbf{r}\rangle)\rangle - 2\frac{\pi e^2}{m_e}k_\rho c^2\omega_0^{-3}\langle\delta n_e(\langle\mathbf{r}\rangle)\delta n_e(\langle\mathbf{r}\rangle)\rangle \ ; \tag{56}$$

$$\frac{d\langle\delta\theta\delta n_e(\langle\mathbf{r}\rangle)}{dt} \simeq \left\langle\delta\theta\frac{\partial\delta n_e(\langle\mathbf{r}\rangle)}{\partial\rho}\right\rangle\frac{d\langle\rho\rangle}{dt} + \left\langle\delta\theta\frac{\partial\delta n_e(\langle\mathbf{r}\rangle)}{\partial\theta}\right\rangle\frac{d\langle\theta\rangle}{dt} + \left(\frac{m^3c^4}{\rho^5}\omega_0^{-3} - 2\frac{mc^2}{\rho^3}\omega_0^{-1}\right)\langle\delta\rho\delta n_e(\langle\mathbf{r}\rangle)\rangle$$

$$- \frac{k_\rho mc^4}{\rho^2}\omega_0^{-3}\langle\delta k_\rho\delta n_e(\langle\mathbf{r}\rangle)\rangle - \left(\frac{m^2c^4}{\rho^4}\omega_0^{-3} + \frac{c^2}{\rho^2}\omega_0^{-1}\right)\langle\delta m\delta n_e(\langle\mathbf{r}\rangle)\rangle$$

$$- 2\frac{\pi e^2}{m_e}\frac{mc^2}{\rho^2}\omega_0^{-3}\langle\delta n_e(\langle\mathbf{r}\rangle)\delta n_e(\langle\mathbf{r}\rangle)\rangle \ ; \tag{57}$$

$$\frac{d\langle\delta k_\rho\delta n_e(\langle\mathbf{r}\rangle)}{dt} \simeq \left\langle\delta k_\rho\frac{\partial\delta n_e(\langle\mathbf{r}\rangle)}{\partial\rho}\right\rangle\frac{d\langle\rho\rangle}{dt} + \left\langle\delta k_\rho\frac{\partial\delta n_e(\langle\mathbf{r}\rangle)}{\partial\theta}\right\rangle\frac{d\langle\theta\rangle}{dt} + \left(\frac{m^4c^4}{\rho^6}\omega_0^{-3} - 3\frac{m^2c^2}{\rho^4}\omega_0^{-1}\right)\langle\delta\rho\delta n_e(\langle\mathbf{r}\rangle)\rangle$$

$$- \frac{k_\rho m^2c^4}{\rho^3}\omega_0^{-3}\langle\delta k_\rho\delta n_e(\langle\mathbf{r}\rangle)\rangle - \left(\frac{m^3c^4}{\rho^5}\omega_0^{-3} - 2\frac{mc^2}{\rho^3}\omega_0^{-1}\right)\langle\delta m\delta n_e(\langle\mathbf{r}\rangle)\rangle$$

$$- 2\frac{\pi e^2}{m_e}\frac{m^2c^2}{\rho^3}\omega_0^{-3}\langle\delta n_e(\langle\mathbf{r}\rangle)\delta n_e(\langle\mathbf{r}\rangle)\rangle - 2\frac{\pi e^2}{m_e}\omega_0^{-1}\left\langle\delta n_e(\langle\mathbf{r}\rangle)\frac{\partial\delta n_e(\langle\mathbf{r}\rangle)}{\partial\rho}\right\rangle \ ; \tag{58}$$

$$\frac{d\langle\delta m\delta n_e(\langle\mathbf{r}\rangle)}{dt} \simeq \left\langle\delta m\frac{\partial\delta n_e(\langle\mathbf{r}\rangle)}{\partial\rho}\right\rangle\frac{d\langle\rho\rangle}{dt} + \left\langle\delta m\frac{\partial\delta n_e(\langle\mathbf{r}\rangle)}{\partial\theta}\right\rangle\frac{d\langle\theta\rangle}{dt} - 2\frac{\pi e^2}{m_e}\left\langle\delta n_e(\langle\mathbf{r}\rangle)\frac{\partial\delta n_e(\langle\mathbf{r}\rangle)}{\partial\theta}\right\rangle \ ; \tag{59}$$

$$\frac{d\left\langle \delta\rho\frac{\partial\delta n_e(\langle\mathbf{r}\rangle)}{\partial\rho}\right\rangle}{dt} \simeq \left\langle \delta\rho\frac{\partial^2\delta n_e(\langle\mathbf{r}\rangle)}{\partial\rho\partial\rho}\right\rangle\frac{d\langle\rho\rangle}{dt} + \left\langle \delta\rho\frac{\partial^2\delta n_e(\langle\mathbf{r}\rangle)}{\partial\rho\partial\theta}\right\rangle\frac{d\langle\theta\rangle}{dt} + \frac{k_\rho m^2c^4}{\rho^3}\omega_0^{-3}\left\langle \delta\rho\frac{\partial\delta n_e(\langle\mathbf{r}\rangle)}{\partial\rho}\right\rangle$$
$$- \left(k_\rho^2c^4\omega_0^{-3} - c^2{\omega_0}^{-1}\right)\left\langle \delta k_\rho\frac{\partial\delta n_e(\langle\mathbf{r}\rangle)}{\partial\rho}\right\rangle - \frac{k_\rho mc^4}{\rho^2}\omega_0^{-3}\left\langle \delta m\frac{\partial\delta n_e(\langle\mathbf{r}\rangle)}{\partial\rho}\right\rangle$$
$$- 2\frac{\pi e^2}{m_e}k_\rho c^2\omega_0^{-3}\left\langle \delta n_e(\langle\mathbf{r}\rangle)\frac{\partial\delta n_e(\langle\mathbf{r}\rangle)}{\partial\rho}\right\rangle \ ; \tag{60}$$

$$\frac{d\left\langle \delta\rho\frac{\partial\delta n_e(\langle\mathbf{r}\rangle)}{\partial\theta}\right\rangle}{dt} \simeq \left\langle \delta\rho\frac{\partial^2\delta n_e(\langle\mathbf{r}\rangle)}{\partial\theta\partial\rho}\right\rangle\frac{d\langle\rho\rangle}{dt} + \left\langle \delta\rho\frac{\partial^2\delta n_e(\langle\mathbf{r}\rangle)}{\partial\theta\partial\theta}\right\rangle\frac{d\langle\theta\rangle}{dt} + \frac{k_\rho m^2c^4}{\rho^3}\omega_0^{-3}\left\langle \delta\rho\frac{\partial\delta n_e(\langle\mathbf{r}\rangle)}{\partial\theta}\right\rangle$$
$$- \left(k_\rho^2c^4\omega_0^{-3} - c^2{\omega_0}^{-1}\right)\left\langle \delta k_\rho\frac{\partial\delta n_e(\langle\mathbf{r}\rangle)}{\partial\theta}\right\rangle - \frac{k_\rho mc^4}{\rho^2}\omega_0^{-3}\left\langle \delta m\frac{\partial\delta n_e(\langle\mathbf{r}\rangle)}{\partial\theta}\right\rangle$$
$$- 2\frac{\pi e^2}{m_e}k_\rho c^2\omega_0^{-3}\left\langle \delta n_e(\langle\mathbf{r}\rangle)\frac{\partial\delta n_e(\langle\mathbf{r}\rangle)}{\partial\theta}\right\rangle \ ; \tag{61}$$

$$\frac{d\left\langle \delta\theta\frac{\partial\delta n_e(\langle\mathbf{r}\rangle)}{\partial\rho}\right\rangle}{dt} \simeq \left\langle \delta\theta\frac{\partial^2\delta n_e(\langle\mathbf{r}\rangle)}{\partial\rho\partial\rho}\right\rangle\frac{d\langle\rho\rangle}{dt} + \left\langle \delta\theta\frac{\partial^2\delta n_e(\langle\mathbf{r}\rangle)}{\partial\rho\partial\theta}\right\rangle\frac{d\langle\theta\rangle}{dt} + \left(\frac{m^3c^4}{\rho^5}\omega_0^{-3} - 2\frac{mc^2}{\rho^3}\omega_0^{-1}\right)\left\langle \delta\rho\frac{\partial\delta n_e(\langle\mathbf{r}\rangle)}{\partial\rho}\right\rangle$$
$$- \frac{k_\rho mc^4}{\rho^2}\omega_0^{-3}\left\langle \delta k_\rho\frac{\partial\delta n_e(\langle\mathbf{r}\rangle)}{\partial\rho}\right\rangle - \left(\frac{m^2c^4}{\rho^4}\omega_0^{-3} - \frac{c^2}{\rho^2}\omega_0^{-1}\right)\left\langle \delta m\frac{\partial\delta n_e(\langle\mathbf{r}\rangle)}{\partial\rho}\right\rangle$$
$$- 2\frac{\pi e^2}{m_e}\frac{mc^2}{\rho^2}\omega_0^{-3}\left\langle \delta n_e(\langle\mathbf{r}\rangle)\frac{\partial\delta n_e(\langle\mathbf{r}\rangle)}{\partial\rho}\right\rangle \ ; \tag{62}$$

$$\frac{d\left\langle \delta\theta\frac{\partial\delta n_e(\langle\mathbf{r}\rangle)}{\partial\theta}\right\rangle}{dt} \simeq \left\langle \delta\theta\frac{\partial^2\delta n_e(\langle\mathbf{r}\rangle)}{\partial\theta\partial\rho}\right\rangle\frac{d\langle\rho\rangle}{dt} + \left\langle \delta\theta\frac{\partial^2\delta n_e(\langle\mathbf{r}\rangle)}{\partial\theta\partial\theta}\right\rangle\frac{d\langle\theta\rangle}{dt} + \left(\frac{m^3c^4}{\rho^5}\omega_0^{-3} - 2\frac{mc^2}{\rho^3}\omega_0^{-1}\right)\left\langle \delta\rho\frac{\partial\delta n_e(\langle\mathbf{r}\rangle)}{\partial\theta}\right\rangle$$
$$- \frac{k_\rho mc^4}{\rho^2}\omega_0^{-3}\left\langle \delta k_\rho\frac{\partial\delta n_e(\langle\mathbf{r}\rangle)}{\partial\theta}\right\rangle - \left(\frac{m^2c^4}{\rho^4}\omega_0^{-3} - \frac{c^2}{\rho^2}\omega_0^{-1}\right)\left\langle \delta m\frac{\partial\delta n_e(\langle\mathbf{r}\rangle)}{\partial\theta}\right\rangle$$
$$- 2\frac{\pi e^2}{m_e}\frac{mc^2}{\rho^2}\omega_0^{-3}\left\langle \delta n_e(\langle\mathbf{r}\rangle)\frac{\partial\delta n_e(\langle\mathbf{r}\rangle)}{\partial\theta}\right\rangle \ ; \tag{63}$$

$$\frac{d\left\langle \delta k_\rho\frac{\partial\delta n_e(\langle\mathbf{r}\rangle)}{\partial\rho}\right\rangle}{dt} \simeq \left\langle \delta k_\rho\frac{\partial^2\delta n_e(\langle\mathbf{r}\rangle)}{\partial\rho\partial\rho}\right\rangle\frac{d\langle\rho\rangle}{dt} + \left\langle \delta k_\rho\frac{\partial^2\delta n_e(\langle\mathbf{r}\rangle)}{\partial\rho\partial\theta}\right\rangle\frac{d\langle\theta\rangle}{dt} + \left(\frac{m^4c^4}{\rho^6}\omega_0^{-3} - 3\frac{m^2c^2}{\rho^4}\omega_0^{-1}\right)\left\langle \delta\rho\frac{\partial\delta n_e(\langle\mathbf{r}\rangle)}{\partial\rho}\right\rangle$$
$$- \frac{k_\rho m^2c^4}{\rho^3}\omega_0^{-3}\left\langle \delta k_\rho\frac{\partial\delta n_e(\langle\mathbf{r}\rangle)}{\partial\rho}\right\rangle - \left(\frac{m^3c^4}{\rho^5}\omega_0^{-3} - 2\frac{mc^2}{\rho^3}\omega_0^{-1}\right)\left\langle \delta m\frac{\partial\delta n_e(\langle\mathbf{r}\rangle)}{\partial\rho}\right\rangle$$
$$- 2\frac{\pi e^2}{m_e}\frac{m^2c^2}{\rho^3}\omega_0^{-3}\left\langle \delta n_e(\langle\mathbf{r}\rangle)\frac{\partial\delta n_e(\langle\mathbf{r}\rangle)}{\partial\rho}\right\rangle - 2\frac{\pi e^2}{m_e}\omega_0^{-1}\left\langle \frac{\partial\delta n_e(\langle\mathbf{r}\rangle)}{\partial\rho}\frac{\partial\delta n_e(\langle\mathbf{r}\rangle)}{\partial\rho}\right\rangle \ ; \tag{64}$$

$$\frac{d\left\langle \delta k_\rho\frac{\partial\delta n_e(\langle\mathbf{r}\rangle)}{\partial\theta}\right\rangle}{dt} \simeq \left\langle \delta k_\rho\frac{\partial^2\delta n_e(\langle\mathbf{r}\rangle)}{\partial\theta\partial\rho}\right\rangle\frac{d\langle\rho\rangle}{dt} + \left\langle \delta k_\rho\frac{\partial^2\delta n_e(\langle\mathbf{r}\rangle)}{\partial\theta\partial\theta}\right\rangle\frac{d\langle\theta\rangle}{dt} + \left(\frac{m^4c^4}{\rho^6}\omega_0^{-3} - 3\frac{m^2c^2}{\rho^4}\omega_0^{-1}\right)\left\langle \delta\rho\frac{\partial\delta n_e(\langle\mathbf{r}\rangle)}{\partial\theta}\right\rangle$$
$$- \frac{k_\rho m^2c^4}{\rho^3}\omega_0^{-3}\left\langle \delta k_\rho\frac{\partial\delta n_e(\langle\mathbf{r}\rangle)}{\partial\theta}\right\rangle - \left(\frac{m^3c^4}{\rho^5}\omega_0^{-3} - 2\frac{mc^2}{\rho^3}\omega_0^{-1}\right)\left\langle \delta m\frac{\partial\delta n_e(\langle\mathbf{r}\rangle)}{\partial\theta}\right\rangle$$
$$- 2\frac{\pi e^2}{m_e}\frac{m^2c^2}{\rho^3}\omega_0^{-3}\left\langle \delta n_e(\langle\mathbf{r}\rangle)\frac{\partial\delta n_e(\langle\mathbf{r}\rangle)}{\partial\theta}\right\rangle - 2\frac{\pi e^2}{m_e}\omega_0^{-1}\left\langle \frac{\partial\delta n_e(\langle\mathbf{r}\rangle)}{\partial\rho}\frac{\partial\delta n_e(\langle\mathbf{r}\rangle)}{\partial\theta}\right\rangle \ ; \tag{65}$$

$$\frac{d\left\langle \delta m \frac{\partial \delta n_e(\langle \mathbf{r} \rangle)}{\partial \rho} \right\rangle}{dt} \simeq \left\langle \delta m \frac{\partial^2 \delta n_e(\langle \mathbf{r} \rangle)}{\partial \rho \partial \rho} \right\rangle \frac{d\langle \rho \rangle}{dt} + \left\langle \delta m \frac{\partial^2 \delta n_e(\langle \mathbf{r} \rangle)}{\partial \rho \partial \theta} \right\rangle \frac{d\langle \theta \rangle}{dt} - 2\frac{\pi e^2}{m_e}\omega_0^{-1} \left\langle \frac{\partial \delta n_e(\langle \mathbf{r} \rangle)}{\partial \theta} \frac{\partial \delta n_e(\langle \mathbf{r} \rangle)}{\partial \rho} \right\rangle ; \quad (66)$$

$$\frac{d\left\langle \delta m \frac{\partial \delta n_e(\langle \mathbf{r} \rangle)}{\partial \theta} \right\rangle}{dt} \simeq \left\langle \delta m \frac{\partial^2 \delta n_e(\langle \mathbf{r} \rangle)}{\partial \theta \partial \rho} \right\rangle \frac{d\langle \rho \rangle}{dt} + \left\langle \delta m \frac{\partial^2 \delta n_e(\langle \mathbf{r} \rangle)}{\partial \theta \partial \theta} \right\rangle \frac{d\langle \theta \rangle}{dt} - 2\frac{\pi e^2}{m_e}\omega_0^{-1} \left\langle \frac{\partial \delta n_e(\langle \mathbf{r} \rangle)}{\partial \theta} \frac{\partial \delta n_e(\langle \mathbf{r} \rangle)}{\partial \theta} \right\rangle . \quad (67)$$

[1] G. Vayakis and C. Walker, "Magnetic diagnostics for iter/bpx plasmas (invited)," *ReviewofScientificInstruments*, vol. 74, no. 4, pp. 2409–2417, 2003.

[2] E. Mazzucato, "Microwave reflectometry for magnetically confined plasmas," *ReviewofScientificInstruments*, vol. 69, p. 2201, 1998.

[3] E. Mazzucato and R. Nazikian, "Effects of turbulent fluctuations on density measurements with microwave reflectometry in tokamaks," *ReviewofScientificInstruments*, vol. 66, p. 392, 1995.

[4] W. H. W. H. Munk, P. Worcester, and C. Wunsch, *Ocean acoustic tomography*. Cambridge University Press, 1995.

[5] J. Strohbehn, "Line-of-sight wave propagation through the turbulent atmosphere," *Proceedings of the IEEE*, vol. 56, no. 8, pp. 1301–1318, 1968.

[6] J. P. S. Bizarro, H. Hugon, and R. Jorge, "Quasilinear approach to ray tracing in weakly turbulent, randomly fluctuating media," *Phys. Rev. A*, vol. 98, p. 023847, Aug 2018.

Expanding the capabilities of REFMUL3

Emanuel Ricardo has a M.Sc. in Engineering Physics in 2014 from Instituto Superior Técnico, Universidade de Lisboa, where he studied the In-vessel Transmission Lines for the ITER Plasma-position Reflectometry Diagnostics System. From 2015 to 2016, he worked in the field of numerical simulation of microwave reflectometry and parallel programming. He started his PhD in 2016 and he is studying the reflectometry diagnostics for DEMO, the first power-generating fusion plasma machine. His work aims to evaluating the behaviour of the reflectometers under DEMO relevant scenarios, taking in account the presence of the blanket modules surrounding the antenna assembly, the vertical movements of the plasma column, the effect of the poloidal divergence for positions away from the equatorial plane and the impact of turbulence and MHD in the measurements.

Emanuel Ricardo

Instituto de Plasmas e Fusão Nuclear (IPFN), Instituto Superior Técnico
Avenida Rovisco Pais, 1049-001 Lisboa, Portugal
E-mail: ericardo@tecnico.ulisboa.pt

Abstract. Numerical simulation plays an important role in the design and assessment of the measurement performance for reflectometers of future fusion machines (eg. ITER and DEMO). REFMUL3 is a 3D FDTD full-wave Maxwell code developed at IPFN and has recently reached the production stage. This code is of great importance for the reflectometry community as a unique tool to cover the full description of a synthetic reflectometer. In this work we developed two important functionalities to be used by the REFMUL3. Firstly, we created C functions to add turbulence to the input plasma electron density. The turbulence is defined by a spectrum and the algorithm computes a RMS normalized fluctuation matrix. The total fluctuations are obtained by applying a frame on the scaled RMS normalized fluctuation matrix, allowing the localization of the turbulence. The functions were implemented and successfully tested for two different spectra. Secondly, we developed CAD2RFM, a program to convert a CAD model to a format compatible with REFMUL3. The algorithm checks if the points of the region of interest are inside of each tetrahedron of a CAD model mesh. This allows the inclusion of complex antennas and structures in the simulations, such as a tokamak's wall. We tested the algorithm by converting successfully a DEMO 2015 baseline scenario CAD model to a structure matrix compatible with REFMUL3.

I. INTRODUCTION

Microwave reflectometry is a plasma diagnostic that makes use of the reflection of electromagnetic waves by a plasma cut-off layer to infer plasma parameters. It is a well known technique to measure electron density profiles in the edge [1]. As a microwave diagnostic, reflectometry fulfills the general diagnostic requirements in the context of a fusion reactor (reduced access, spatial and temporal resolution, robustness) [2]. The mathematical model behind reflectometry assumes a plane wave propagating in a cold and one-dimensional inhomogeneous plasma. However, in a real reflectometer there are three fundamental aspects that have impact on the measurement performance. Firstly, real reflectometers are composed by a system of antennas with complicated surrounding structures, resulting in non ideal radiation patterns. Secondly, the emitted signal is reflected in the plasma and part of it interacts with the tokamak's wall. This results in multiple plasma/wall reflections that can be later detected by the antenna. Thirdly, the plasma is an extremely complex medium. A real plasma has curvature, turbulence and can move and be deformed during a discharge. Hence, the use of a synthetic reflectometer plays an essential role in the design and assessment of the measurement performance of reflectometers for the future machines such as ITER and DEMO.

One of the most popular numerical techniques to simulate microwave reflectomentry is the finite-difference time-domain (FDTD). REFMUL3 is a 3D FDTD full-wave Maxwell code developed at IPFN (parallelized under the EURATOM High Level Support Team) and has recently reached the production stage. REFMUL3 is of great importance for the reflectometry community as a tool to cover the full 3D description of a reflectometer. Unlike REFMULF, a 2D FDTD full-wave Maxwell code also developed at IPFN, REFMUL3 is proper to study the amplitude of the detected signal because all the field components of the probing beam are taken in account. The effects of the three dimensional description of the plasma and of the surrounding structure in the detected wave phase are also of great interest [3][4].

In this work we developed two important functionalities to be used by REFMUL3 in the future simulations. Firstly, we created C functions to define turbulence in the input plasma electron density. The turbulence is defined by a spectrum and the algorithm computes the IDFT with the FFTW library [5] to create a RMS normalized fluctuation matrix. The turbulent component of the total density is obtained by applying a frame to the scaled RMS normalized matrix, allowing the localization of the turbulence. This functionality is described in the section II. Secondly, we develop a program to convert a CAD file to a format compatible with REFMUL3. This allows the inclusion of complex structures in the simulations, such as a tokamak's wall. This functionality is described in the section III.

II. INCLUDING TURBULENCE IN THE REFMUL3

The electron density of a turbulent plasma is described by

$$n_e(x,y,z) = n_0(x,y,z) + \delta n_e(x,y,z) \tag{1}$$

where $n_e(x,y,z)$ is the total density, $n_0(x,y,z)$ is the averaged density and $\delta n_e(x,y,z)$ the fluctuations. In REFMUL3, the plasma electronic density is defined by a 3D matrix with $N_x \times N_y \times N_z$ elements. N is the number of elements for the respective dimension. The space between two consecutive points, dx, depends on the frequency used to define the FDTD grid. We defined a linear averaged density $n_0(x,y,z)$ in a $699 \times 499 \times 499$ grid, with initial position located at $x_0 = 250$ and a cut-off density of $1.1164 \times 10^{19}\ m^{-3}$ (30 GHz) at $x_s = 450$. The fluctuations are described by a spectrum with the form

$$S_T(\mathbf{k}) = |S_T(\mathbf{k})| \exp\left[i\phi(\mathbf{k})\right] \tag{2}$$

where $\mathbf{k} = (k_x, k_y, k_z)$ is the wave vector and the phase $\phi(\mathbf{k})$ is random. The $|S_T(\mathbf{k})|$ function is usually taken in the form $|S_T(\mathbf{k})| = S(k_x)S(k_y)S(k_z)$ form, where $S(k)$ is the one dimensional turbulence spectrum. To test the algorithm, we implemented a one dimensional turbulence spectrum in the form

$$S(k) = \frac{1}{a_0 + \sum_{j=1}^{N_o} |a_j k s|^j} \tag{3}$$

where a_j are the coefficients, s the scaling factor and N_o the order. This function is frequently used to model the plasma turbulence. In order to test the functions and based in the previous studies for ITER [6], we defined two different spectra using $N_o = 3$, $a_0 = 1$, $a_1 = 0.005$, $a_2 = 0$ and $a_3 = 0.001875$, with different scaling values, $s = 1$, and $s = 8$. By increasing the scaling factor, we have sharper peaks, meaning shorter wave numbers and consequently higher wavelengths in our fluctuations (larger structures). After applying the inverse Fourier transform and obtaining the n_e^S matrix, we normalize it to its root mean square. Thus the RMS normalized density fluctuation matrix is

$$\delta n_e^{\mathrm{RMS}} = \frac{\delta n_e^S}{\mathrm{RMS}(\delta n_e^S)} \tag{4}$$

With this definition, most of the elements are in the $[-1, 1]$ range, so we can scale it to the desired value, keeping the fluctuations spectra. Figure 1 shows the RMS normalized density fluctuation matrix for the two cases, calculated with the FFTW IDFT algorithm. The contour plot is in the [0,4] range.

The total density fluctuation matrix is defined as

$$\delta n_e(i,j,k) = \mathrm{lvl} \times \mathrm{Frm}(i,j,k) \times N \times \delta n_e^{\mathrm{RMS}}(i,j,k) \tag{5}$$

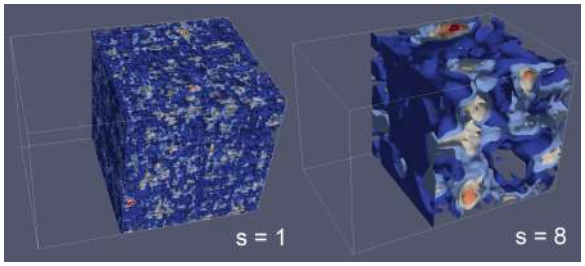

FIG. 1: example of RMS normalized density fluctuations

where i, j, k are the matrix indexes for the x, y, and z dimensions, lvl is the turbulence level (0-100%), Frm is a frame matrix in the 0-1 range, N is the density corresponding to Frm= 1 and lvl= 100%, and $\delta n_e^{\mathrm{RMS}}$ the RMS normalized density fluctuations. With the goal of localize the fluctuations in the cutoff position, we defined a Gaussian frame Frm in the form

$$\mathrm{Frm}(i,j,k) = \mathrm{Frm}(i) = \exp\left(-\frac{(i-x_s)^2}{2\sigma^2}\right) \qquad (6)$$

where σ is σ_1 before x_s and σ_2 after. In order to apply the frame to our example, we defined $\sigma_1 = 20$ and $\sigma_2 = 60$. Figure 2 shows the result of applying the frame to the RMS normalized fluctuation matrix.

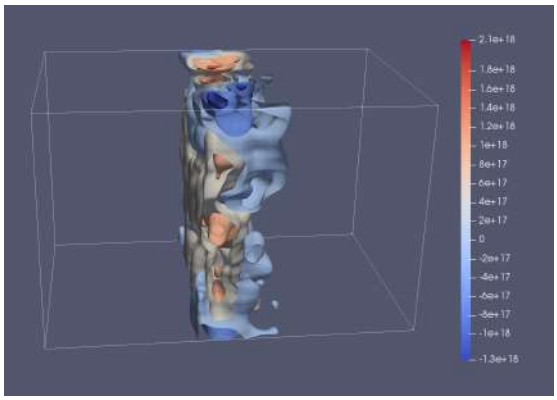

FIG. 2: Normalized density with the Gaussian frame applied.

By using this framed density fluctuation matrix, we calculated the total density, shown in figure 3. When we sum the two components of the total density, we take in account that some of the entries can become negative. Thus we check if it is negative and we set it to zero in case of needed.

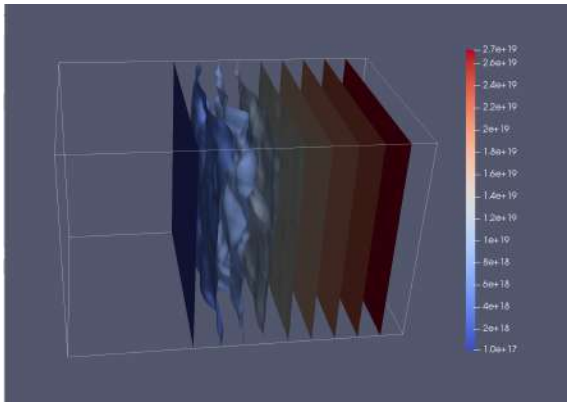

FIG. 3: Total density for the $s = 8$ spectrum

III. CONVERTING CAD MODELS TO A FORMAT COMPATIBLE WITH REFMUL3

A. The conversion algorithm

In REFMUL3, a perfect metallic structure is also defined by a three dimensional matrix, here called the structure matrix. This matrix has two values, the 0 is defined at the structure and the 1 is defined at the vacuum. Given a CAD model, we were interested in converting a region of interest (ROI), the volume to be simulated, in one structure matrix. The ROI box is defined by an initial and final position in each dimension. The corresponding grid has $N_x \times N_y \times N_z$ elements, each point equally spaced by dx, which, as mentioned, depends on the used frequency to define the FDTD grid. In this context, the program CAD2RFM was written in C. The algorithm converts a tetrahedron mesh of a CAD model to a structure matrix and finds the necessary source parameters to excite the radiation in the desired x position. For the selected box, we can also select a plane to obtain a 2D model to be used by the REFMULF. The program supports the REFMUL3 data structures, command-line argument parsing, output file formats (HDF5) and data types (FLOAT or DOUBLE). Thus, its functions can be directly implemented in the REFMUL3 code.

The conversion algorithm is described by two main operations, the frame conversion and the CAD model conversion. In the first operation, the coordinates of all the mesh nodes are converted in case of needed. This operation is very useful since REFMUL3 excites the electromagnetic field in the yz plane. Thus, if we have a complex model such as the wall of a tokamak with several antennas in different positions with specific orientations, we need to align the ROI box with the intended emitting structure. The S frame is defined such that it is aligned with the orientation of the ROI. By aligning them, we make sure the emission is performed in the desired plane. If the CAD model is defined in another frame S', the coordinates of the nodes that define the tetrahedrons must

be converted to the S frame before the algorithm of conversion. Defining p_S as the coordinates of the point p in the S frame, $p_{S'}$ represents the coordinates of the same point in the S' frame. Thus, the relation between the coordinates of both frames is

$$p_S = p_o + R\, p_{S'} \tag{7}$$

where p_o is the origin of the S with coordinates given in the S' frame and R the rotation matrix, given by

$$R = \begin{bmatrix} v_{xx} & v_{yx} & v_{zx} \\ v_{xy} & v_{yy} & v_{zy} \\ v_{xz} & v_{yz} & v_{zz} \end{bmatrix} \tag{8}$$

with

$$v_j = \frac{p_j - p_o}{\sqrt{|p_j - p_o|^2}} \tag{9}$$

p_j are the coordinates of points located at the j axis ($j = x, y, z$), given in the S' frame. Since we want to convert the data from frame S' to the S frame, the algorithm uses equation (7) in the form

$$p_S = R^{-1}\,(p_{S'} - p_o) \tag{10}$$

In the second operation, the CAD model is converted for a structure matrix. Initially, the CAD model is converted to a mesh of tetrahedrons, composed by a list of nodes and a tetrahedron list described by a set of the four tetrahedron vertices. The conversion of the mesh to a structure matrix is composed by 3 steps that are performed for every tetrahedron. The basic operation is to check if a given point p of the ROI is inside of a given tetrahedron or not. By doing this operation for all the points inside the ROI we fill the tetrahedron volume. The operation consists in five different steps, described as follows:

- We assume a tetrahedron as shown in figure 4.

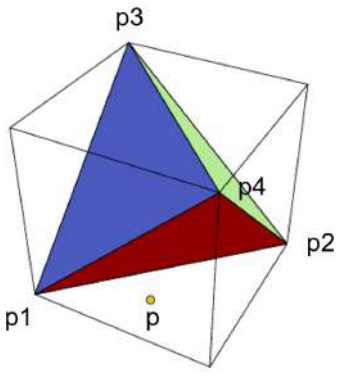

FIG. 4: Tetrahedron scheme

  The tetrahedron is composed by 4 different nodes (p1,p2,p3,p4). This gives 4 different planes: (p1,p2,p3), (p1,p2,p4), (p1,p3,p4) and (p2,p3,p4). As example, we select one of them, the (p1,p2,p3) one.

- Using the three points, we find the a, b and c parameters of the respective plane equation:

$$ax + by + cz + d = 0 \tag{11}$$

- Then we use the other point of the tetrahedron, in this example, the p4, to find the d parameter. This parameter will have a given sign.

- We do the same, but with the test point p. If the d parameter has the same signal as the $p4$, that means that they are in the same side.

- We do the same procedure for the other planes. If the reference point is always at the same side as the different reference points, this means that the point p is inside the tetrahedron. The structure is initialized in vacuum, so if the point is inside the tetrahedron its value is changed for the metallic structure one.

If the tetrahedron is inside the ROI, we find the cube with lower volume that contains it, as represented in figure 4. Thus we don't need to check all the points of the region of interest, only those contained in the cube, reducing the computational time. Before applying this procedure for a given tetraedron, we check if it is in the ROI or not. If not, we do not convert this tetrahedron and analyze the next one. With this algorithm we can convert any CAD model to a structure matrix with any dimensions defined by a region of interest.

B. Testing CAD2RFM

In order to test the CAD2RFM conversion algorithm, we created a simple CAD model of a tokamak's wall, giving a width of 1600 mm and a thickness of 100 mm to the 2D model of the DEMO 2015 wall. This model is currently being used to study the reflectometry measurements at 16 different positions. One of the fundamental aspects of this study is aligning the antennas with the separatrix, so we expect a lower plasma curvature effect in the measurement [6]. The antennas were designed in the respective locations and with the respective orientations. Figure 5 shows the respective CAD model (with a representation of the plasma) and the respective mesh.

Then we used CAD2RFM to create a structure matrix for the gap 9, located at the top of the machine. We defined a ROI aligned with the antenna (excitation is performed in a plane) as represented in the figure 5 (the blue box), with dimensions $1m \times 0.8m \times 0.8m$ and a grid of $1000 \times 800 \times 800$ points. The obtained structure matrix is shown in figure 6. As expected, the antenna is aligned with the ROI and the wall is now converted to the antenna's frame.

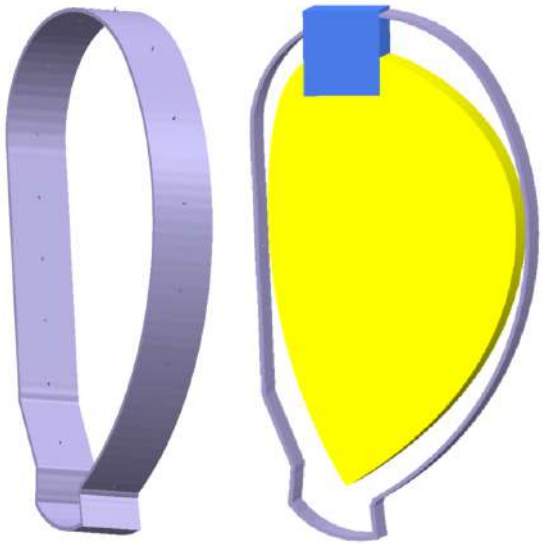

FIG. 5: The DEMO model and the ROI defined in the GAP 9

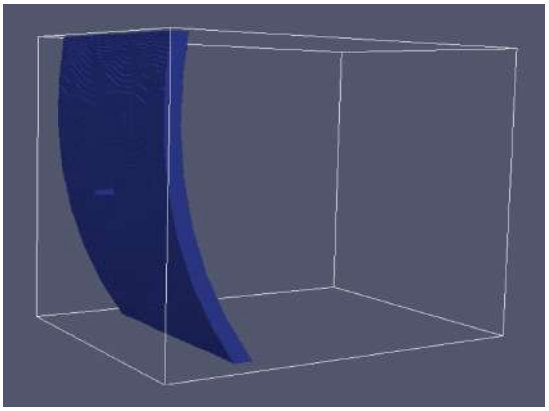

FIG. 6: Obtained structure matrix for the GAP 9

With these examples we observed the capability of CAD2RFM in converting complex CAD models to a structure matrix compatible with REFMUL3.

IV. CONCLUSIONS

Numerical simulation is fundamental in the design and assessment of the measurement performance of the reflectometers for the future machines such as ITER and DEMO. In this work we developed two important functionalities to be used by the REFMUL3, a 3D FDTD full-wave Maxwell code developed at IPFN. This code is of great importance for the reflectometry community as a tool to cover the full description of a synthetic reflectometer. REFMUL3 is proper to study the amplitude of the detected signal because all the field components of the probing beam are taken in account. The effects of the three dimensional description of the plasma and of the surrounding structure is also of great interest.

Firstly, we created C functions to add turbulence to the input plasma electron density. The turbulence is defined by a spectrum and the algorithm computes the IDFT with the FFTW library to create a RMS normalized fluctuation matrix. The turbulent component of the density is obtained by applying a frame to the scaled RMS normalized matrix, allowing the localization of the turbulence. The functions were implemented and successfully tested for two different spectra with different scales of turbulence. Then we localized the fluctuations in the cut-off position of a linear density profile and obtained the total density matrix. This functionality is fundamental in the study of the beam-plasma interaction. The turbulence plays an important role in the signal losses and in the detection of a wrong time round-trip delay. We can take advantage of the FFWT-GSL libraries for real-complex data transforms.

The second functionality that we introduced was CAD2RFM, a program to convert a CAD model to a format compatible with REFMUL3. The algorithm checks if the points of the region of interest are inside of each tetrahedron of a CAD model mesh. We tested the algorithm by converting successfully a DEMO 2015 baseline scenario CAD model with the antennas designed perpendicularly to the separatrix to a structure matrix compatible with REFMUL3. All the functions were created with the REFMUL3 data structures and file formats so they can be easily internally directly implemented. The process of checking all the tetrahedrons can be parallelized, decreasing the conversion computational time. CAD2RFM allows the inclusion of complex structures such as a tokamak's wall in the future REFMUL3 simulations, being an essential functionality to obtain the full description of a reflectometer.

[1] E. Mazzucato, "Microwave imaging reflectometry for the visualization of turbulence in tokamaks," *Nuclear Fusion*, vol. 41, pp. 203–213, feb 2001.
[2] T. G. H. Hartfuß, *Fusion Plasma Diagnostics with mm-Waves*. 2013.
[3] T. R. F. da Silva, S. Heuraux, "Introducing refmulf, a 2d full polarization code and refmul3, a 3d parallel full wave maxwell code," *International Reflectometry Workshop IRW 13*, 2017.
[4] F. da Silva; S. Heuraux; S. Hacquin; M.E. Manso, "Unidirectional transparent signal injection in finite-difference time-domain electromagnetic codes –application to reflec-

tometry simulations," *Journal of Computational Physics*, vol. 203, 2005.

[5] S. Frigo, M.; Johnson, "The design and implementation of fftw3," *Proceedings of the IEEE*, vol. 93, 2005.

[6] S. H. A. S. E. Ricardo, F. da Silva, "Assessment of a multi-reflectometers positioning system for demo plasmas," *12º Congresso do Comité Português da URSI*, 2018.

Recent developments on electronics for magnetic diagnostic in nuclear fusion devices

André Torres obtained his Masters Degree in Engineering Physics by IST in the year of 2017. A science and technology enthusiast since an early age, his curiosity for how things work led him to physics and he found in nuclear fusion a scientific field where physics and cutting-edge engineering meet. This led him to the Munich for an Erasmus exchange at TUM and to Barcelona for a traineeship at Fusion For Energy, where he conducted his master thesis work on magnetic diagnostic electronics and real-time data distribution.

André Torres

Instituto de Plasmas e Fusão Nuclear (IPFN), Instituto Superior Técnico
Avenida Rovisco Pais, 1049-001 Lisboa, Portugal
E-mail: andregtorres@tecnico.ulisboa.pt

Abstract. Magnetic diagnostic plays a key role in magnetic fusion devices diagnostic sets. The signal generated by electromagnetic induction in coils of different shapes and positions needs to be integrated in real-time in order to be able to feed plasma shape and position control loops. This requires fast, stable and reliable electronics that keep integration drift to a minimum. Inaccurate measurements would lead to wrong inputs to the control system which could put the safe operation of the device at risk. While conventionally achieved by analogue integrators, developments in analogue and digital electronics made digital integration viable. This article describes the development of such systems for a selection of devices, detailing key improvements to this field made in the last years and possible shortcomings of the designs.

I. INTRODUCTION

Being one of the fundamental diagnostics in fusion devices, inductive magnetic diagnostic consists of a number of probes, coils and loops with different geometries and in different toroidal and poloidal positions. Based on electro-magnetic induction, these coils have a signal proportional to the magnetic flux rate of change. To access the magnetic field, there is the need to integrate this signal. This integration is conventionally done with analogue integrators. This process is prone to drifts – a small DC component added to the signal that after integrated results in a slope along time in the measurement. With the discharge time of fusion devices increasing on route to continuous operation, long pulse integration is a major technological challenge for magnetic diagnostic developers. A requirement of keeping the drift bellow 500 $^{-}$V s was set for ITER [1]. This requirement is not achieved by any system currently in operation and led to the adoption of digital integration, a technique only made possible by recent developments in Field Programmable Gate Arrays (FPGA) and Analogue to Digital Converter (ADC) improvements over the last decades.

This review is collects the publish architectures that are used in medium to large sized fusion devices. This means that (i) it is divided and structured by devices; (ii) experimental systems that were successfully developed and tested but did not see full implementation, such as the long pulse hybrid integrator in DIII-D [2], are not included; (iii) major devices such as JET or ASDEX-U are absent since their systems are similar to the ones presented, yet older and with fewer technical innovations published.

The following sections detail the magnetic diagnostic electronics in a selection of devices, highlighting its key features, and in a generally chronological order with the last two being the current state-of-the-art – analog and digital integration. Last section summarizes and draws conclusions from the trend and evolution of the research on this topic.

II. JT-60

JT-60 developed a different integrator based on Voltage to Frequency Converters (VFC) and Up-Down Counters (UDC) [3]. This strategy works according to the following principle (see Fig. 1): the linear VFC converts the probe measurement voltage into a square pulse wave of a varying frequency. This digital signal is compared with the externally provided reference (0 V equivalent frequency) and counted in the UDC working at a 8 MHz clock (counting) frequency. The output of the counter is therefore digital and is connected to the DAS or to a Digital Signal Processor (DSP) in case further processing is needed. This method requires signal conditioning in order to make sure the signal is constrained in the input range of the VFC. This strategy makes use of complex

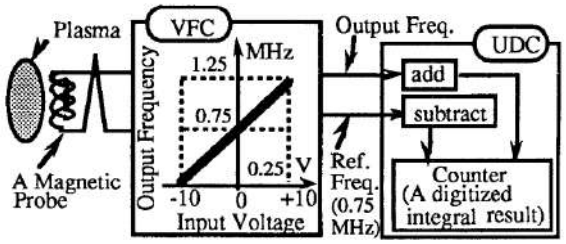

FIG. 1: JT-60 VFC-UDC digital integrator schematic [3].

electronics, introducing several problems:

- **VFC (non-)linearity**. Component dependent.
- **Deadbands** (mV) produced at singular frequencies (1/n, n=2,3,...) of the clock frequency introduced by the Phase Locked Loop (PLL) phenomenon. The approach to mitigate this effect was to isolate the analog and digital parts in different boards through photo-couplers and cooling of the boards.
- **Varying drift rates**. Problems identified due to ground fluctuations due to several reference voltage sources.
- **Stepped change** at high frequency and high voltage phenomena (plasma instabilities, breakdown, termination, disruptions). Usage of attenuators possible with decreased SN ratio and large drift introduced. Possible solution using parallel integration paths proposed.

III. DIII-D (ANALOG)

The most recent integrators in DIII-D are analog. As common practice in such devices, they feature a differential input and drift compensation (see Fig. 2). This compensation includes a "coarse manual adjustment" plus a track-and-hold circuit with feedback that collects the integral value in between shots and holds it at the beginning of the shot. This technique ensures a very long integration time for the drift compensation. Another correction applied before integration is the compensation for the toroidal flux for the diamagnetic loop, with an analog adder at the input of the boards.

Unlike other analog integrator circuits, it has a splitting of the power in order to accommodate a no-integration parallel path. While providing the non integrated data, this technique is technically difficult to realize and can degrade the quality of the diagnostic data (from experience in JET recounts).

Another relevant feature of the electronics is the daily monitoring and calibration of the integration gain $\frac{G}{RC}$ with the integration of a standard square waveform.

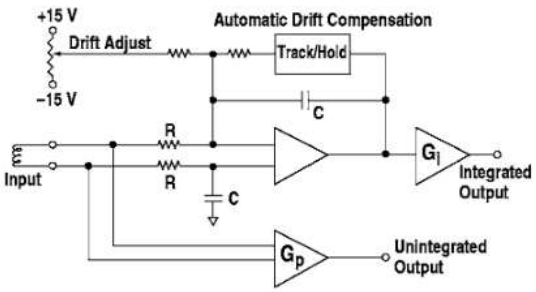

FIG. 2: Schematic representation of the analog integrator for DIII-D [4].

As for the digital acquisition systems and CODAC, DIII-D has a PCI interconnects with control cycles of 50 ¯s, 250 ¯s running on Xenon 2.4 GHz computers (see Fig. 3).

IV. KSTAR

KSTAR uses a analog integrator with drift compensation developed in 2007. An uncommon feature of the electronics developed is the conditioning stages before and after the long transmission line. This was done due to the low input resistance of the integrator (1 kΩ) and the 100m long transmission line attenuation and RF noise pick up. In between the signal cable there is a transmitter and receiver module. The transmitter ts of a Pi filter a surge protector (1 kV) and an instrumentation amplifier. The signal is then made differential for the transmission line and the receiver based on another differential amplifier, removing the unwanted non-symmetric components and leading then to the integrator (see Fig. 4).

The integrator is not differential and instead of a S&H

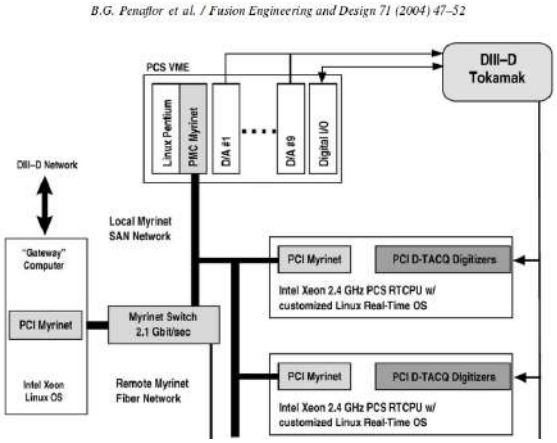

FIG. 3: Schematic representation of the DIII-D DAS and real-time control architecture [5].

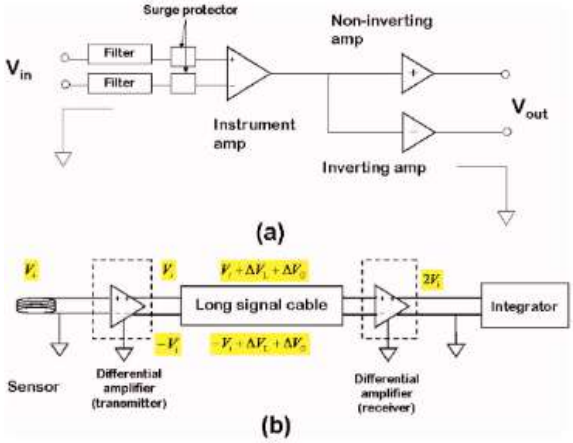

FIG. 4: Schematic representation of the transmitter (a) path from the sensors to the integrators (b) [6].

circuit, uses the digitalized signal to compensate the drift. The output of the integrating Op Amp goes to an external digitizer and to an ADC (see Fig. 5). The now digital signal is saved in two registers [6]. Register B goes to a PC for monitoring and data display (RS-232) and register A to a DAC that feeds back to the integrator input for the drift compensation [7].

V. TORE SUPRA

The integrator in Tore Supra (2000) was considered the state of the art in analog integration as per the ITER magnetics conceptual design. It mas use of a differential input structure with two symmetrical integration cells (Fig. 6). Like other analog integrators, it has automatic drift compensation trough a modified integrating S&H circuit with the hold capacitor as feedback [8]. The development of these integrators payed attention to the following aspects:

- "Zero drift" OP Amps.
- Polypropylene capacitors with low leakage current.

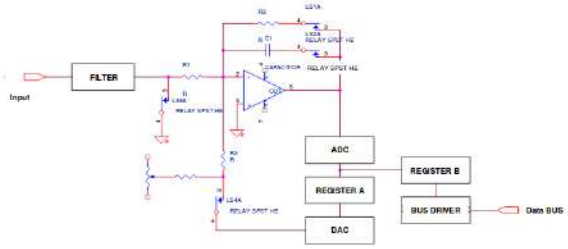

FIG. 5: Schematic representation of the analog integrator in KSTAR with Pi filter and ADC-register-DAC mechanism for drift compensation [7].

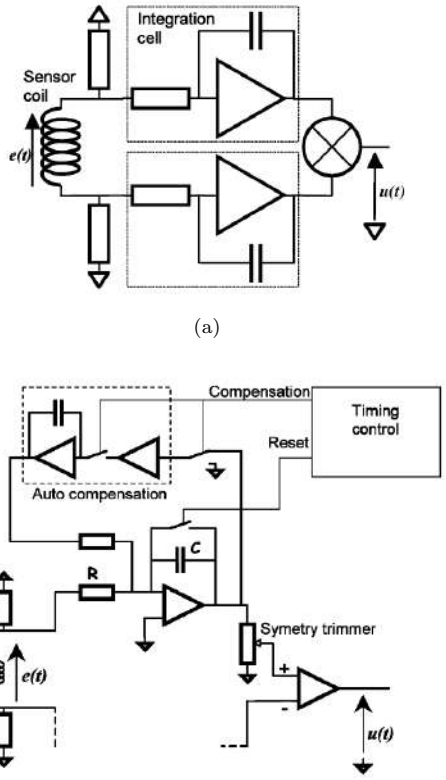

FIG. 6: Schematic representation of the analog integrators in Tore Supra [8]. (a) Dual integration cell differential structure. (b) Cell scheme.

- Integrator based auto compensation S&H circuit with similar technology capacitor.
- S&H circuit with no feedback when in hold mode. This prevents the OP Amp from reaching saturation and increasing the local temperature.
- Relays with high open switch insulation
- Earth-screen PCB layer.
- Trim resistor to adjust the symmetry between the two cells.

This design is similar to the COMPASS integrators (1995).

VI. WEST

The integrators currently in WEST are an evolution of the Tore Supra electronics. Two prototypes (Fig. 7) were developed in collaboration with IPR (India). One of the prototypes focuses on improvements on the analog drift compensation while another prototype has a digital

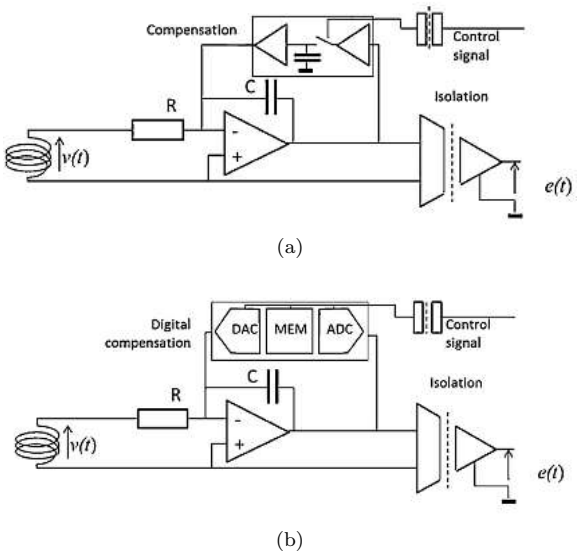

FIG. 7: Schematic representation of the analogue integrators in WEST [9]. (a) Analogue S&H compensation. (b) Digital compensation.

strategy (ADC-DAC) for the compensation. Additionally, these integrators get rid of the dual integration path in order to remove the tuning requirements due to the increased number of integrators. Another motivation for the upgrade was to have a lighter command-control system with a single digital state to all integrators [9]. The biggest technical improvement is the galvanic insulation of the signal and power supplies, as a way of increasing the Common Mode Rejection Ratio (CMRR). Both prototypes show improvements over the old Tore Supra integrators.

VII. W-7X

For the W7-X stellarator, with predicted experiments up to 30 minutes in duration, the approach for the integration for the magnetic diagnostics was digital [10]. The motivation for this disruptive change is the minimization of the drift, due to the long acquisition times.

Besides acquiring the signal with the ADC before integration, the key component in this architecture is the square wave modulation of the signal through a chopper. The chopper consists of CMOS switches used to invert the polarity of the signal at the clock frequency. This technique requires an associated low-pass filter as preconditioning (Fig. 8). The filter ensures that there is no high frequency transient during the switch by spreading the energy in a larger time interval, keeping the integral unaltered (introducing latency). The implemented filter has the cutoff frequency at around 150 Hz. The signal is thereafter modulated by a square waveform by the chopper. This technique allows the removal of DC or low fre-

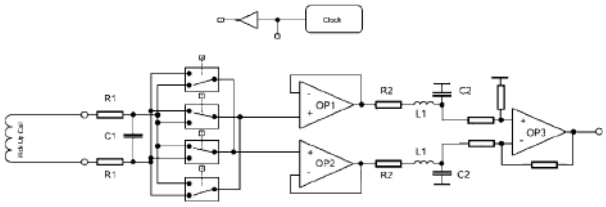

FIG. 8: Schematic representation of the analog part of the digital chopper integrator for W7-X [10].

quency components introduced between modulation and demodulation, which includes the noise added by several biased components, prone to compensation problems. Fig. 9 shows, step-by-step, the effect the (de)modulation has on a constant offset introduced in the electronics. This technique is well established, having been tested in WEGA and EAST [10, 11], presently used in ISTTOK and W7-X [12, 13] and selected for the ITER magnetic diagnostic integrators, also developed at IPFN [14, 15].

After the necessary conditioning for the ADC input and digitalization, it is demodulated and integrated in the FPGA on a Advanced Telecommunications Computing Architecture (ATCA) board. This has one major advantage: keeping both demodulated[18] and integrated signals (in real-time). The ATCA board fits 32 channels with a single FPGA. It is a variation of IPFN ATCA-MIMO-ISOL with a simplified Rear Transmission Module (RTM) with only digital I/O channels [16].

VIII. CONCLUSIONS

Performance, particularly drift mitigation has been increasing over the years. This was achieved by the availability of more accurate electrical components with better performance and by a series of incremental and disruptive innovations. There is a noticeable trend of simplification of electrical circuits. This is motivated by the already referred performance increase on the electrical components available and by the emphasis on galvanic insulation. The evolution of the Tore Supra into WEST integrators is a good example of both these phenomena.

The advancements on ADC technology makes the introduction of digital electronics predominant in newly commissioned systems. Even if based in analogue integration, digital electronics for drift compensation (ADC-DAC feedback) has been validated as an effective automatic drift compensation technique. However, digital integration is gaining more strength in the scientific community after the successful results in W7-X and its adoption for ITER. Despite its motivator being the long pulse integration, its increased flexibility and adaptability (with possibility of firmware reprogramming) over analogue electronics makes it advantageous even for experiments with shorter pulse lengths. It is currently operated in ISTTOK and tests of this solution were conducted in EAST. The latest results from KSTAR [17] show that despite the solution described in this review having had a good performance in an initial stage, after the introduction of hot-wall operation in a recent campaign, the drift increased drastically. The resistivity increase of the coils with temperature made the integrators input impedance too low, leading the magnetic diagnostic team to conclude the system needs to be replaced by digital integrators.

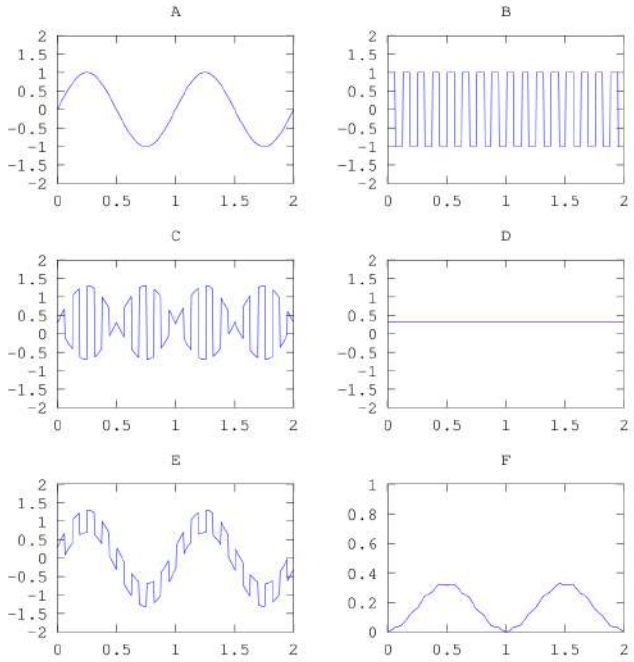

FIG. 9: Effect of the modulation and demodulation technique on a sinusoidal signal (A) modulated by the chopper signal (B) with a constant offset (D) added to the modulated signal. The modulated signal (C) is digitalized and on the FPGA it is demodulated (E) and integrated (F).

[1] A. C. Neto, S. Arshad, F. Sartori, G. Vayakis, G. Ambrosino, A. Batista, I. Bas, R. Campagnolo, B. B. Carvalho, G. D. Magneval, G. D. Tommasi, O. Dominguez, J. L. Fernandez-Hernando, A. Pironti, S. Simrock, J. Sousa, C. Sterle, A. Vergara, A. Winter, and L. Zabeo, "Conceptual architecture of the plant system controller for the magnetics diagnostic of the ITER tokamak," *Fusion Engineering and Design*, vol. 96–97, pp. 887–890, 2015.

[2] E. J. Strait, J. D. Broesch, R. T. Snider, and M. L. Walker, "A hybrid digital–analog long pulse integrator," *Review of Scientific Instruments*, vol. 68, no. 1, pp. 381–

384, 1997.

[3] K. Kurihara and Y. Kawamata, "Development of a precise long-time digital integrator for magnetic measurements in a tokamak," in *17th IEEE/NPSS Symposium Fusion Engineering (Cat. No.97CH36131)*, vol. 2, pp. 799–802 vol.2, Oct 1997.

[4] E. J. Strait, "Magnetic diagnostic system of the diii-d tokamak," *Review of Scientific Instruments*, vol. 77, no. 2, p. 023502, 2006.

[5] B. Penaflor, J. Ferron, R. Johnson, and D. Piglowski, "Current status of the upgraded diii-d real-time digital plasma control system," *Fusion Engineering and Design*, vol. 71, no. 1, pp. 47 – 52, 2004. 4th IAEA Technical Meeting on Control, Data Acquistion, and Remote Participation for Fusion Research.

[6] J.-G. BAK, S. Lee, D. Son, and E. M Ga, "Analog integrator for the korea superconducting tokamak advanced research magnetic diagnostics," *The Review of scientific instruments*, vol. 78, p. 043504, 05 2007.

[7] J.-G. BAK, S. Lee, E. M Ga, and D. Son, "Integrator for the kstar magnetic diagnostics," vol. 2, 01 2005.

[8] P. Spuig, P. Defrasne, G. Martin, M. Moreau, P. Moreau, and F. Saint-Laurent, "An analog integrator for thousand second long pulses in tore supra," *Fusion Engineering and Design - FUSION ENG DES*, vol. 66, pp. 953–957, 09 2003.

[9] P. Spuig, P. Kumari, M. Moreau, P. Moreau, A. Le-luyer, and P. Malard, "Enhanced integrators for west magnetic diagnostics," *Fusion Engineering and Design*, vol. 96-97, pp. 966 – 969, 2015. Proceedings of the 28th Symposium On Fusion Technology (SOFT-28).

[10] A. Werner, "W7-x magnetic diagnostics: Performance of the digital integrator," *Review of Scientific Instruments*, vol. 77, no. 10, p. 10E307, 2006.

[11] Y. Wang, Z. S. Ji, G. J. Xu, F. Wang, S. Li, X. Y. Sun, and Z. C. Zhang, "A digital long pulse integrator for EAST Tokamak," in *Fusion Engineering and Design*, 2014.

[12] D. Corona, N. Cruz, J. J. E. Herrera, H. Figueiredo, B. B. Carvalho, I. S. Carvalho, H. Alves, and H. Fernandes, "Design and Simulation of ISTTOK Real-Time Magnetic Multiple-Input Multiple-Output Control," *IEEE Transactions on Plasma Science*, vol. 46, no. 7, pp. 2362–2369, 2018.

[13] M. Endler, B. Brucker, V. Bykov, A. Cardella, A. Carls, F. Dobmeier, A. Dudek, J. Fellinger, J. Geiger, K. Grosser, O. Grulke, D. Hartmann, D. Hathiramani, K. Höchel, M. Köppen, R. Laube, U. Neuner, X. Peng, K. Rahbarnia, K. Rummel, T. Sieber, S. Thiel, A. Vorköper, A. Werner, T. Windisch, and M. Ye, "Engineering design for the magnetic diagnostics of wendelstein 7-x," *Fusion Engineering and Design*, vol. 100, pp. 468 – 494, 2015.

[14] A. J. N. Batista, "F4E prototype of a chopper digital integrator for the ITER magnetics," in *SOFT*, 2016.

[15] A. J. Batista, G. Naylor, L. Capellà, A. Neto, A. Stephen, N. Petrella, S. Hall, J. Sousa, B. Carvalho, F. Sartori, R. Campagnolo, I. Bas, B. Gonçalves, S. Arshad, G. Vayakis, S. Simrock, and L. Zabeo, "Testing results of chopper based integrator prototypes for the ITER magnetics," *Fusion Engineering and Design*, vol. 128, pp. 193–197, mar 2018.

[16] B. B. Carvalho, A. Batista, M. Zilker, K. Rahbarnia, and W.-X. C. Team, "Design, implementation and commissioning of atca based high-speed multichannel data acquisition systems for magnetic diagnostics in w7-x," in *11th IAEA Technical Meeting on Control, Data Acquisition, and Remote Participation for Fusion Research, Greifswald*, 2017.

[17] K. Heung-Su and J.-G. Bak, "Effect of temperature on magnetic measurements in kstar tokamak,"

[18] Note that these signals are filtered with a low frequency LP filter. The main application of these boards is control. In order to recover the high frequency signal, ITER boards have a parallel path without this filter (10 Hz cutoff).

Review of Compact Objects Relativistic Magnetospheres

Rui Torres was born in 1994 in Lisbon, Portugal. He started as an intern at the theory and simulation team of Group of Lasers and Plasmas (GoLP)/IPFN to investigate the role of 6-photon scattering processes in the polarization of vacuum. He obtained his MSc degree in Engineering Physics at Instituto Superior Técnico, Universidade de Lisboa (IST/UL). The topic of his MSc thesis was realistic modeling of vacuum polarization induced light scattering scenarios in extreme intense fields under the supervision of Professor Luís O. Silva and Dr. Thomas Grismayer. Thereupon, he was awarded a grant to further study the effects of an imperfect vacuum or imperfect electromagnetic pulses in the characterization of the QED signatures induced. Currently, his Ph.D. work intends to explore magnetosphere dynamics of rotating compact objects with general relativistic considerations.

Rui Torres

Instituto de Plasmas e Fusão Nuclear (IPFN), Instituto Superior Técnico
Avenida Rovisco Pais, 1049-001 Lisboa, Portugal
E-mail: `rui.t.torres@tecnico.ulisboa.pt`

Abstract. The quest to explain the most violent events in the Universe and the corresponding emitted radiation spectrum has led the community to explore the properties of plasma-filled magnetospheres of compact objects. These magnetospheres are complex systems that engage quantum electrodynamic(QED) processes, kinetic-scale pair plasma physics and general relativity (GR).

To study such intricate and exotic systems, advanced simulation techniques are required. Combining multidimensional parallel particle-in-cell (PIC) simulations with dedicated modules to tackle microscopic physical processes allows for a complete description of global magnetospheres. However, these global models are very demanding from a computational point of view, requiring access to supercomputating resources. These detailed simulations capable of identifying key particle acceleration mechanisms may play a role in decoding the experimentally observed radiation spectrum.

The gravitational frame dragging effects in macroscopic plasma dynamics in the vicinity of compact objects, such as neutron stars and rotating black holes, may now be accessible through the development of a novel GR-PIC module. A self-consistent study of the magnetospheric plasma surrounding these compact objects may unveil the interlacing and eventual interplay between the microscopic and the macroscopic processes.

I. INTRODUCTION

Just over one hundred years ago, Einstein developed the theory of general relativity, showing how gravity can be seen as the curvature of the spacetime fabric. This theory revealed that the Universe is an extreme place populated with regions where the space-time is so wrapped that it can trap even light (see Fig. 1). Compact objects responsible for such distortions are designated as black holes, and play a role in the most violent space events, such as active galactic nuclei (AGN) jets and gamma-ray bursts [1]. During such events, enormous amounts of energy are released. There are several possible explanations: gravitational collapse leading to a new black hole, gravitational energy released during the accretion of a compact object onto an existing black hole, or rotational energy of the black hole being imparted to the surrounding matter [2]. Due to the extreme and complex nature of such compact objects, they combine sub-fields as general relativity, plasma astrophysics and quantum mechanics. For this reason, they comprise extraordinary physics laboratories. However, there are still many unanswered questions regarding their formation and evolution. Ongoing campaigns such as the Event Horizon Telescope [3, 4] and GRAVITY [5, 6], target the supermassive black hole at the center of our own galaxy and M87, in a quest to resolve horizon-scale structures. In order to interpret data flowing in from these experiments, global models of the black holes and their active magnetospheres must be self-consistently studied. The understanding of the electromagnetic evolution of these objects leads to the comprehension of the acceleration mechanisms in such exotic plasma environments. Ultimately, this has the potential to unravel a plethora of phenomenology, ranging from black hole rotational energy extraction to the Penrose process [7] in general Blandford-Znajek jets [8].

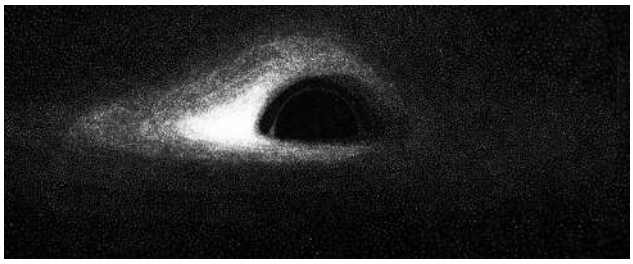

FIG. 1: Depiction of what a flat disc of material falling into a black hole might look like if we were close enough to see it. The intense gravity of the black hole bends light around it. For this reason, the flat disc seems to be deformed [9].

II. FROM NEUTRON STAR TO BLACK HOLE MAGNETOSPHERES

The observation of rapidly pulsating radio sources [10, 11] led the community to conduct the first global studies of pulsar magnetospheres. The aligned rotator model was studied by Goldreich and Julian (*GJ*, 1969), showing that a rotationally induced electric field due to the star rotation could pull charged particles from its surface [12]. In this way, a magnetosphere would be filled with plasma. This *ab initio* vacuum solution for the rotating neutron star was addressed using the force-free approximation [1] and resulted in the discovery that an electromagnetically driven wind could extract rotational energy and angular momentum from the star. The latter process is usually designated as neutron star spin-down. In 1974, Wald discovered a solution of the vacuum Maxwell's equations in Kerr space-time coordinates [13]. This solution predicted that rotating black holes could also support strong electromagnetic fields. In a similar way to the aligned rotator, Blandford and Znajek (1977) showed that there was the possibility of driving an electromagnetic wind from a black hole if a plasma supply was assured by its magnetosphere [14]. They argued that the vacuum solution was unstable to pair production cascades, thus providing the magnetospheric plasma required. Once again, and through the application of the force-free approximation, they have studied the temporal evolution of the magnetic field lines of a rotating black hole. As the plasma rotates within the black hole ergosphere [1], the field lines that are frozen into it are dragged, forcing the field lines to wind around into giant helices that spiral out along the black hole rotational axis (see Fig. 2 and 3). This process is usually designated as the Blandford-Znajek mechanism and explains how plasma-filled magnetospheres mediate the extraction of black hole rotational energy and the launching of a relativistic jet [14].

III. NUMERICAL METHODS

The Blandford-Znajek mechanism is often studied using a fluid approximation for the plasma allied with the force-free approximation, the force-free magnetohydrodynamics (MHD). These numerical codes have been used lately to model global dynamics of pulsars [15–18] and black holes [8, 19], ranging from resistive and full relativistic MHD [20–22], to describing the motion of a magnetized fluid in curved spacetime (GRMHD) [23, 24]. While MHD models have leveraged the understanding of black hole accretion and jet production, by accurately describing the transfer of energy from the spinning black hole to the magnetic field, and by retriving jet parameters directly from the black hole spin. However, considering the plasma as a continuous fluid leads to the loss of important kinetic details of the system. Such kinetic treatment is required to track par-

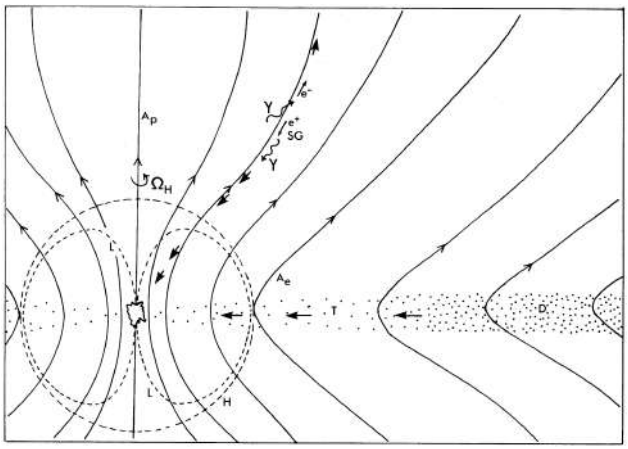

FIG. 2: Schematic cross-section of a rotating black hole and corresponding magnetosphere. H represents the event horizon. Magnetospheric plasma currents drag the magnetic field lines that are initially aligned with the black hole rotation axis. Inside the black hole ergosphere, the plasma co-rotates with the compact object. In this way, magnetic field lines wind around into giant helices that spiral out of the accretion disk plane [1, 14].

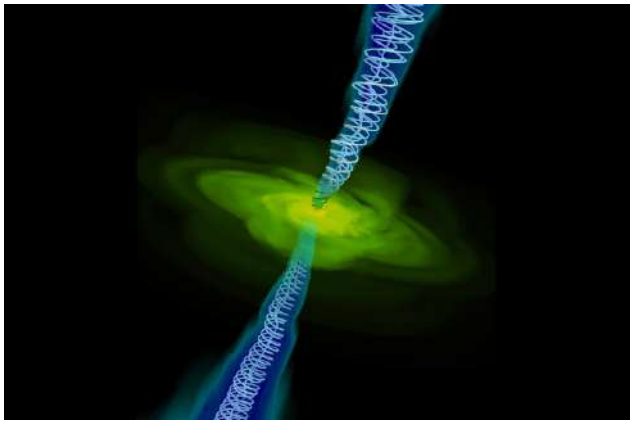

FIG. 3: An artist's depiction of a black hole with two opposing jets. The black hole is surrounded by a cloud of infalling gas (green), while the jets are defined by spiraling magnetic field lines (blue). Credits: Alexander Tchekhovskoy at Lawrence Berkeley National Laboratory

ticle acceleration mechanisms that lead to the observed radiation spectrum and the generation of secondary particles [10, 11]. In addition, these models do not take into account pair production, radiation reaction in ultra-intense electromagnetic fields and other quantum electrodynamic (QED) processes. In this way, it precludes them from correctly taking into account the formation of the magnetospheric plasma, jet's mass loading and predicting the observed radiation and accelerated particle spectrum. The latest computational advances enabled the first fully kinetic simulations of pulsar and black hole magnetospheres [25, 26]. These simulations make use of an axisymmetric configuration which is the most tractable to tackle the problem at hand. These simulations are two-[25, 27] and three-[28, 29] dimensional, and may also take into consideration pair production [30] or general relativity [24, 26]. In [31], the kinetic modeling of the electromagnetic dissipation mechanism in two pulsar magnetosphere mergers was studied. This work shows that a non-repeating fast radio burst can be a precursor of gravitational waves due to the magnetosphere coalescence. At Grupo de Lasers e Plasmas [32], Instituto de Plasmas e Fusão Nuclear [33], a similar study of the aligned rotator in [25] was performed. These simulations present a state-of-the-art charge conserving scheme allied with a QED module that properly takes into account the local interaction of the particles with the ultra-intense fields, allowing for an *ab initio* modeling of global pulsar magnetospheres via improved phenomenological models. New studies suggest that the lack of polar cap activity in low inclination pulsars does not agree with observations, hinting that frame dragging effect may increase the local value of the parallel component of the electric field (in relation to the magnetic field). The increase of the unscreened electric field amplitude accelerates magnetospheric plasma particles and lead to the ignition of the discharge [24, 29, 30] (see Fig. 4).

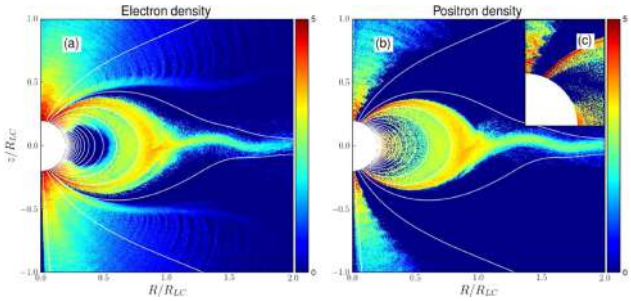

FIG. 4: The inclusion of GR effects excites pair production in the aligned pulsar magnetosphere configuration. This enhancement allows the activation of the pulsar polar cap. White lines represent magnetic field lines and the plasma densities are represented by a logarithmic color scheme (normalized to the GJ density at the pole). Panels (a) and (b) show electron and positron densities, respectively. Panel (c) shows a zoom of the positron density close to the neutron star surface [24].

IV. NEW CHALLENGES

To tackle these GR effects, a new module that extends the previous work to curve space-time configurations is required. The space-time immediately surrounding a real neutron star will have significant Schwarchild-like curvature, producing an appreciable frame-dragging effect. As it was already mentioned, this general relativity considerations can lead to an increase in the unscreened parallel electric field component, which enhances the radiation of gamma-photons required to produce pairs and, ultimately, to populate the pulsar magnetosphere [24].

The role of curved space-time in *ab initio* modeling of global pulsar magnetospheres may be identified in a self-consistent way. In addition, this new module will enable the study of black hole magnetospheric dynamics, unraveling the role of the ergosphere in the rotational energy and angular momentum extraction mechanisms, jet launching and accretion disk formation [1, 26]. Massively parallel Particle-in-Cell (PIC) simulations are ideally suited to model global black hole magnetospheres as they can resolve spatiotemporal kinetic scales of pair plasmas, self-consistently describe the unscreened electric field, particle acceleration, pair production and support the emission of observable radiation.

ACKNOWLEDGMENT

This work was supported by Fundação para a Ciência e Tecnologia (grant PD/BD/142971/2018).

[1] S. S. Komissarov, "Electrodynamics of black hole magnetospheres," *Monthly Notices of the Royal Astronomical Society*, vol. 350, pp. 427–448, 05 2004.

[2] D. Christodoulou, "Reversible and irreversible transformations in black-hole physics," *Phys. Rev. Lett.*, vol. 25, pp. 1596–1597, Nov 1970.

[3] S. S. Doeleman, J. Weintroub, A. E. E. Rogers, R. Plambeck, R. Freund, R. P. J. Tilanus, P. Friberg, L. M. Ziurys, J. M. Moran, B. Corey, K. H. Young, D. L. Smythe, M. Titus, D. P. Marrone, R. J. Cappallo, D. C. J. Bock, G. C. Bower, R. Chamberlin, G. R. Davis, T. P. Krichbaum, J. Lamb, H. Maness, A. E. Niell, A. Roy, P. Strittmatter, D. Werthimer, A. R. Whitney, and D. Woody, "Event-horizon-scale structure in the supermassive black hole candidate at the galactic centre," *Nature*, vol. 455, pp. 78 EP –, 09 2008.

[4] S. S. Doeleman, V. L. Fish, D. E. Schenck, C. Beaudoin, R. Blundell, G. C. Bower, A. E. Broderick, R. Chamberlin, R. Freund, P. Friberg, M. A. Gurwell, P. T. P. Ho, M. Honma, M. Inoue, T. P. Krichbaum, J. Lamb, A. Loeb, C. Lonsdale, D. P. Marrone, J. M. Moran, T. Oyama, R. Plambeck, R. A. Primiani, A. E. E. Rogers, D. L. Smythe, J. SooHoo, P. Strittmatter, R. P. J. Tilanus, M. Titus, J. Weintroub, M. Wright, K. H. Young, and L. M. Ziurys, "Jet-launching structure resolved near the supermassive black hole in m87," *Science*, vol. 338, no. 6105, pp. 355–358, 2012.

[5] N. Hamaus, T. Paumard, T. Müller, S. Gillessen, F. Eisenhauer, S. Trippe, and R. Genzel, "Prospects for testing the nature of SgrA*'s near-infrared flares on the basis of current very large telescope and - future very large telescope interferometer - observations," *The Astrophysical Journal*, vol. 692, pp. 902–916, feb 2009.

[6] GRAVITY Collaboration, "First light for gravity: Phase referencing optical interferometry for the very large telescope interferometer," *A&A*, vol. 602, p. A94, 2017.

[7] R. Penrose, "Gravitational Collapse: the Role of General Relativity," *Nuovo Cimento Rivista Serie*, vol. 1, 1969.

[8] J. C. McKinney, "Total and jet blandford-znajek power in the presence of an accretion disk," *The Astrophysical Journal*, vol. 630, pp. L5–L8, aug 2005.

[9] J.-P. Luminet, "Seeing black holes: From the computer to the telescope," *Universe*, vol. 4, no. 8, 2018.

[10] A. Hewish, S. J. Bell, J. D. H. Pilkington, P. F. Scott, and R. A. Collins, "Observation of a rapidly pulsating radio source," *Nature*, vol. 217, no. 5130, pp. 709–713, 1968.

[11] F. Pacini, "Energy emission from a neutron star," *Nature*, vol. 216, no. 5115, pp. 567–568, 1967.

[12] P. Goldreich and W. H. Julian, "Pulsar Electrodynamics," *The Astrophysical Journal*, vol. 157, p. 869, Aug. 1969.

[13] R. M. Wald, "Black hole in a uniform magnetic field," *Phys. Rev. D*, vol. 10, pp. 1680–1685, Sep 1974.

[14] R. D. Blandford and R. L. Znajek, "Electromagnetic extraction of energy from Kerr black holes," *MNRAS*, vol. 179, pp. 433–456, May 1977.

[15] A. Gruzinov, "Power of an axisymmetric pulsar," *Phys. Rev. Lett.*, vol. 94, p. 021101, Jan 2005.

[16] A. N. Timokhin, "On the force-free magnetosphere of an aligned rotator," *Monthly Notices of the Royal Astronomical Society*, vol. 368, pp. 1055–1072, 04 2006.

[17] A. Spitkovsky, "Time-dependent force-free pulsar magnetospheres: Axisymmetric and oblique rotators," *The Astrophysical Journal*, vol. 648, pp. L51–L54, aug 2006.

[18] J. Pétri, "The pulsar force-free magnetosphere linked to its striped wind: time-dependent pseudo-spectral simulations," *Monthly Notices of the Royal Astronomical Society*, vol. 424, pp. 605–619, 07 2012.

[19] S. Koide, "Magnetic extraction of black hole rotational energy: Method and results of general relativistic magnetohydrodynamic simulations in kerr space-time," *Phys. Rev. D*, vol. 67, p. 104010, May 2003.

[20] J. Li, A. Spitkovsky, and A. Tchekhovskoy, "Resistive solutions for pulsar magnetospheres," *The Astrophysical Journal*, vol. 746, p. 60, jan 2012.

[21] S. S. Komissarov, "Simulations of the axisymmetric magnetospheres of neutron stars," *Monthly Notices of the Royal Astronomical Society*, vol. 367, pp. 19–31, 03 2006.

[22] A. Tchekhovskoy, A. Spitkovsky, and J. G. Li, "Time-dependent 3D magnetohydrodynamic pulsar magnetospheres: oblique rotators," *Monthly Notices of the Royal Astronomical Society: Letters*, vol. 435, pp. L1–L5, 08 2013.

[23] C. F. Gammie, J. C. McKinney, and G. Toth, "HARM: A numerical scheme for general relativistic magnetohydrodynamics," *The Astrophysical Journal*, vol. 589, pp. 444–457, may 2003.

[24] A. A. Philippov, B. Cerutti, A. Tchekhovskoy, and A. Spitkovsky, "Ab initio pulsar magnetosphere: The role of general relativity," *The Astrophysical Journal*, vol. 815, p. L19, dec 2015.

[25] A. Philippov, A. Spitkovsky, K. Parfrey, and B. Cerutti, " Particle acceleration in axisymmetric pulsar current sheets," *Monthly Notices of the Royal Astronomical Society*, vol. 448, pp. 606–619, 02 2015.

[26] K. Parfrey, A. Philippov, and B. Cerutti, "First-principles plasma simulations of black-hole jet launch-

ing," *Phys. Rev. Lett.*, vol. 122, p. 035101, Jan 2019.
[27] M. A. Belyaev, "Dissipation, energy transfer, and spin-down luminosity in 2.5D PIC simulations of the pulsar magnetosphere," *MNRAS*, vol. 449, pp. 2759–2767, May 2015.
[28] A. A. Philippov and A. Spitkovsky, "Ab initio pulsar magnetosphere: Three-dimensional particle-in-cell simulations of axisymmetric pulsars," *The Astrophysical Journal*, vol. 785, p. L33, apr 2014.
[29] A. A. Philippov, A. Spitkovsky, and B. Cerutti, "Ab initio pulsar magnetosphere: Three-dimensional particle-in-cell simulations of oblique pulsars," *The Astrophysical Journal*, vol. 801, p. L19, mar 2015.
[30] A. Y. Chen and A. M. Beloborodov, "Electrodynamics of axisymmetric pulsar magnetosphere with electron-positron discharge: A numerical experiment," *The Astrophysical Journal*, vol. 795, p. L22, oct 2014.
[31] B. Crinquand, B. Cerutti, and G. Dubus, "Kinetic modeling of the electromagnetic precursor from an axisymmetric binary pulsar coalescence," *Accepted in Astronomy & Astrophysics*, vol. arXiv:1812.05898 [astro-ph.HE], Dec 2018.
[32] "Grupo de Lasers e Plasmas." `http://golp.tecnico.ulisboa.pt/`.
[33] "Instituto de Plasmas e Fusão Nuclear." `https://www.ipfn.tecnico.ulisboa.pt/`.

Calculation of transport coefficients for fluid modelling of atmospheric pressure plasma jets

Duarte was born in Madeira island, Portugal, in 1994. He moved to Lisbon to study Engineering Physics at IST where he received is MSc degree in 2017 by implementing an electron-impact ionization module for the LisbOn KInetics (LoKI) code, under the project KIT-PLASMEBA. Afterwards, he continued his research in low-temperature plasmas by including a non-linear module dealing with electron-impact ionization and electron-electron collisions, and with the implementation and validation of a Helium kinetic scheme for LoKI. After entering the APPLAuSE program in 2018, he joined the N-PRiME group of IPFN, where he will perform aerodynamic studies of atmospheric pressure plasma jets. He enjoys seeing new places while trekking and camping, and can make a reasonable poncha.

Duarte Gonçalves

Instituto de Plasmas e Fusão Nuclear (IPFN), Instituto Superior Técnico
Avenida Rovisco Pais, 1049-001 Lisboa, Portugal
E-mail: duarte.b.goncalves@tecnico.ulisboa.pt

Abstract. Atmospheric pressure plasma jets have recently attracted much attention in a wide range of applications, which led to the development of experiments and computational simulations. For the latter, a promising method is the use computational fluid dynamic (CFD) codes with consistent reaction mechanisms.

For reactive flows, the viscosity and diffusion coefficients must take into account the transport of a chemical species within all other species. For non-thermal equilibrium plasmas, the conductivity coefficients must be calculated for every non-equilibrium temperature being considered. While the Chapman/Enskog procedure provides an accurate framework for the calculation of transport coefficients, its application in CFD is computationally expensive. An alternative is to apply different simplifications. The Wilkie/Blottner/Eucken and Gupta/Yos models try to solve this problem, with the latter being more accurate but needing more input parameters that may not be available for every gas mixture.

Electron diffusion velocity may become very high, due to the low electron mass, which may lead to the violation of the quasi-neutrality assumption or unrealistic chemical non-equilibrium. This can be solved with an implementation of ambipolar diffusion.

I. INTRODUCTION

Cold Atmospheric Pressure Plasma Jets (APPJ) have recently attracted much attention [1–4] due to the possibility of propagating non-thermal plasmas in open air at ambient pressure and temperature, delivering reactive plasma species (e.g. radicals, ions, UV radiation), in addition to long-living afterglow species, to targets located some centimetres away from the main discharge zone. This property enables the development of a wide range of new and promising applications, e.g. in biomedicine and healthcare, chemical analysis, or material processing.

Modelling the different physical scales of APPJ is significantly complex and extremely challenging. It requires combining computational fluid dynamics with plasma physics / chemistry models, to capture the processes occurring in the discharge, and downstream when the APPJ interacts with the surrounding flow conditions. One of the approaches is the development of a Computational Fluid Dynamics (CFD) code, with self-consistent particle and energy source terms representing the APPJ features [5].

Low temperature APPJs are in Non-Local Thermal Equilibrium (NLTE), not only between electrons and heavy species, but also within the atoms and molecules internal degrees of freedom. This leads to the definition of various temperatures (translational, electronic, vibrational, rotational, excitation), which may be global or in respect to an individual species. Furthermore, the chemical activity of these plasmas means that a number of species must be considered. As a result, the fluid model to be translated into a CFD code should include reactive terms and non-equilibrium energy terms properly coupled. This leads not only to an increase in the number of conservation equations to be solved but also in the complexity of the coefficients being used.

In the fluid model equations, diffusive terms (transport terms due to microscopic interactions) need at least three transport coefficients as input parameters, which are usually pressure and temperature dependent. Inclusion of various species, with different transport properties, means that new effective transport coefficients must be calculated. As a result, NLTE means that the effective transport coefficients have to be calculated in real-time for every cell of the computational domain during the CFD simulation [6].

Because of that, the use of the accurate, but computationally expensive, Chapman-Ensok procedure [7] becomes prohibitive. Simpler models, derived from the Chapman-Ensok solution, are usually used, with the Wilke/Blottner/Eucken and Gupta/Yos model being described in this work. Section II introduces the basic formalism of a fluid modelling for non-equilibrium reactive flows. Section III defines the various diffusive terms to be calculated. Section IV describes two models used to calculate transport coefficients in weakly ionized gases. And finally Section V concludes with final remarks.

Various physical quantities are used in this text which are not always defined the first time they appear in the equations. Table I contains a description of these symbols.

TABLE I: List of symbols

Symbol	Units	Description
ρ	kg m^{-3}	Mass density
c_i	-	Mass fraction
J	kg m^{-2}s^{-1}	Mass diffusion flux
$\dot{\omega_i}$	kg m^{-3}s^{-1}	Mass source term
$[\tau]$	N m^{-2}	Viscous stress tensor
P	Pa	Pressure
ϵ_k	J kg^{-1}	Internal energy
h	J kg^{-1}	Specific Enthalpy
q_{C_k}	J m^{-2}s^{-1}	Conduction heat flux
$\dot{\omega_k}$	J m^{-3}s^{-1}	Energy source term
D_i	m^{-2}s^{-1}	Diffusion coefficient
μ	kg m^{-1}s^{-1}	Viscosity coefficient
λ	J s^{-1}m^{-1}K^{-1}	Thermal conductivity
T	K	Temperature
x_i	-	Molar fraction
M_i	kg mol^{-1}	Molar mass
C_V	J kg^{-1} K^{-1}	Specific heat c. volume
C_P	J kg^{-1} K^{-1}	Specific heat c. pressure
R_u	mol^{-1}	Universal gas constant
k_B	J mol^{-1}	Boltzmann constant

II. FLUID MODELLING OF REACTIVE FLOWS

Fluid models can be constructed by coupling various approximations of the Boltzmann Transport Equation (BTE). This equation describes the time variation of a given species i probability density function f_i in the six-dimensional phase space,

$$\frac{\partial f_i}{\partial t} +_i \cdot \nabla_r f_i + q_i(E + v_i \times B) \cdot \nabla_{v_i} f_i - \sum_{k \neq i} \int \int (f_i' f_k' - f_i f_k)||v_i - v_k||\sigma_{ik} dv_k d\omega = 0. \quad (1)$$

By calculating the various velocity moments of the Boltzmann equation one can obtain the fluid conservation equations. A moment of order l can be calculated by multiplying the BTE by $(mv)^l$ and integrating in the velocity space. The zeroth order moment leads to the mass conservation equation, also known as continuity equation; the first moment leads to the momentum conservation equation; and the second moment leads to the energy conservation equation.

A complete description would have N_{spe} Boltzmann equations for each of the N_{spe} species being considered. It

is usual to solve the momentum conservation equation for the total density and assuming that every species moves with the same velocity, leading to only one momentum conservation equation. Also, in the case of thermal equilibrium one total energy conservation equation is solved, while in non-thermal equilibrium the energy equation is solved for the various energetic degrees of freedom.

Ignoring electromagnetic effects, a self-consistent fluid model for a flow with N_{spe} reactive species and N_{temp} energy degrees of freedom described by a non-equilibrium temperature, would use a set of fluid conservation equations constituted by: N_{spe} mass conservation equations,

$$\frac{\partial}{\partial t}(\rho c_i) + \nabla \cdot (\rho u c_i) = \nabla \cdot J_i + \dot{\omega}, \tag{2}$$

in which $i = \{1, 2, ..., N_{spe}\}$; one momentum conservation equation,

$$\frac{\partial}{\partial t}(\rho u) + \nabla \cdot (\rho u \otimes u) = \nabla \cdot [\tau] - \nabla P; \tag{3}$$

and n energy conservation equations,

$$\frac{\partial}{\partial t}(\rho \epsilon_k) + \nabla \cdot (\rho u h_k) = \nabla \cdot \left(q_{C_k} + \sum_i J_i h_{i,k} + \dot{\omega}_k, \right) \tag{4}$$

in which $k = \{1, 2, ..., N_{temp}\}$

Each of these equations are constituted by transient ($\partial\psi/\partial t$), advective ($\nabla \cdot (\psi u)$), diffusive ($\nabla \cdot \xi$), and reactive terms, in which ψ is one of the flow variables [ρc_i, ρu, $\rho \epsilon_k$], ξ one of the diffusive fluxes (see Table II), and the reactive terms the source terms due to the creation and destruction of particles.

III. CALCULATION OF DIFFUSIVE TERMS

In the previous equations we can see that the divergence of the mass diffusive fluxes J_i, the stress tensor $[\tau]$, and the heat conduction fluxes q_{C_k} define the diffusive terms. These concern dissipative processes, which is the natural transport of mass, momentum, and energy by the random motion and collisions of the gas particles at a microscopic level. Each of these diffusive fluxes is described by constitutive relations.

General formulations of mass diffusion fluxes require the solution of the Stefan-Maxwell equations [8]. These form a system of linear equations which can become quite computationally expensive to solve. The simplest and most widely used formulation of mass diffusion fluxes is Fick's law [9],

$$J_i = \rho D_i \nabla(c_i), \tag{5}$$

although its accuracy maybe limited in some cases [9].

The standard expression for the viscous stress tensor [9] is used. Assuming a Newtonian fluid and the Stokes hypothesis for the normal stresses,

$$[\tau] = \mu \left(\nabla u + (\nabla u)^T \right) - \frac{3}{2} \mu (\nabla \cdot u)[I]. \tag{6}$$

The heat conduction flux, for every non-equilibrium temperature, can be described by Fourier's law,

$$q_{C_k} = \lambda_k \nabla T_k. \tag{7}$$

Using these constitutive relations our diffusive fluxes are described by a transport coefficient times a gradient of the relevant variable, see Table II. With this choice of constitutive relations, the transport coefficients characterize the response of the gas to gradients in concentration, velocity, and temperature.

TABLE II: Dissipative fluxes and transport coefficients

	Diffusive flux	Transport coeff.	Gradient
Mass diffusion	J_i	D_i	∇c_i
Viscosity	$[\tau]$	μ	$\nabla \cdot u$
Thermal conductivity	q_{C_k}	λ_i	∇T_k

IV. CALCULATION OF TRANSPORT COEFFICIENTS

The transport coefficients are function of the pressure, temperature, and chemical composition of the flow. Due to the non-equilibrium nature of weakly ionized plasmas, all of these quantities may have strong spatial variations, meaning that the computation of the transport coefficients must be done in real time during a CFD simulation [6].

Accurate transport coefficients may be provided by the Chapman-Ensok procedure[7], valid for small Knudsen numbers. This procedure implies the solution of a linear system of equations which can lead to unreasonable computation times. A less demanding approach is the use of approximate mixture rules that allow the calculation of effective transport coefficients. Most of these rules come from simplifications of the Chapman-Enskog solution.

A. Wilke/Blottner/Eucken model

This model was developed by Wilke [10], and consists in a first order Chapman-Enskog relation. Here a global viscosity coefficient μ is calculated along with thermal conductivity coefficients λ_k for every global temperature T_k. These are given by Wilke's semi-empirical mixing rule,

$$\mu = \sum_i \frac{x_i \mu_i}{\phi_i}, \tag{8}$$

$$\lambda_k = \sum_i \frac{x_i \lambda_{ik}}{\phi_i}. \tag{9}$$

Here x_i is the species molar fraction and ϕ_i are weights calculated with molar mass M_i fractions between every species,

$$\phi_i = \sum_r x_r \left[1 + \left(\frac{\mu_i}{\mu_r}\right)^{1/2} \left(\frac{M_r}{M_i}\right)^{1/4}\right]^2 \left[8\left(1 + \frac{M_i}{M_r}\right)\right]^{-1/2} \tag{10}$$

The individual viscosities are calculated using the Blottner model [11]

$$\mu_i(T) = 0.1 \exp\left[(A_i \ln T + B_i) \ln T + C_i\right], \tag{11}$$

in which μ_i is in $[\mathrm{kgm^{-1}s^{-1}}]$, T is the species translational temperature in kelvin, and A_i, B_i, and C_i are fitting coefficients.

The individual thermal conductivities for each degree of freedom λ_{ik} is determined using the generalized Eucken's relation [12], using a unit Schmidt number,

$$\begin{aligned}
\lambda_{i,tra} &= \frac{5}{2}\mu_i \; C_{Vtra,i} \\
\lambda_{i,rot} &= \mu_i \; C_{Vrot,i} \\
\lambda_{i,vib} &= \mu_i \; C_{Vvib,i} \\
\lambda_{i,exc} &= \mu_i \; C_{Vexc,i}.
\end{aligned}$$

in which $C_{Vmode,i}$ is the individual specific heat at constant volume for a given mode which is given by,

$$\begin{aligned}
C_{Vtra,i} &= \frac{3}{5} C_{Ptra,i} = \frac{3}{2} r_i \\
C_{Vrot,i} &= C_{Prot_i} = r_i \\
C_{Vvib,i} &= C_{Pvib_i} = \frac{\partial \epsilon_{vib,i}}{\partial T_{vib,i}} \\
C_{Vexc,i} &= C_{Pexc_i} = \frac{\partial \epsilon_{exc,i}}{\partial T_{exc,i}}
\end{aligned}$$

in which $C_{Pmode,i}$ is the individual specific heat at constant pressure, $r_i = k_B/m_i$ being the species gas constant, and m_i the species mass.

The mass diffusion coefficients are a single binary diffusion coefficient D,

$$D = \frac{L_e \lambda}{\rho C_P} \tag{12}$$

in which a constant Lewis number is used $L_e = 1.2$, C_P is the mixture total specific heat at constant pressure of the gas mixture.

The biggest advantage of this model is its low number of input parameters, which makes it suitable for most gas mixtures. Some concerns exist for temperature above 10 000 K [13], see Figure 1 and 2, which is not the case of cold APPJs. Although it is simpler it is only 5%-10% faster than the Gupta/Yos model [6].

B. Gupta/Yos collision cross-section model

In this model formulated by Gupta et al. [14] a simplification of the Chapman-Enskog solution proposed by Yos [15] is used. The model contains further simplifications, valid for weakly ionized gases, to reduce the computation time. The formulation is similar to Wilke's but it considers the corresponding collision cross-sections between each pair of species.

In this model two interaction strengths $\Delta^1_{i,r}$ and $\Delta^2_{i,r}$ are used for each pair of species i, r,

$$\Delta^1_{i,r} = \frac{8}{3}\left[\frac{2 M_i M_r}{\pi R_u T_c (M_i + M_r)}\right]^{1/2} \pi \bar{\Omega_{ir}}^{1,1}(T_c) \tag{13}$$

and equivalently $\Delta^2_{i,r}$ using $\bar{\Omega_{ir}}^{2,2}$, in which $\pi\bar{\Omega^{1,1}_{ir}}$ and $\pi\bar{\Omega^{2,2}_{ir}}$ are average collision cross sections, or collisional integrals, calculated using Gupta's curve fits [14]. The controlling temperature T_c is the translation temperature of the heavy species with the exception of electron-impact interaction in which the electron temperature is used.

The gas mixture viscosity is evaluated using the mixing rule,

$$\mu = \sum_i \frac{x_i m_i}{\sum_r x_r \Delta^2_{ir}}. \tag{14}$$

The translational thermal conductivity for heavy species is evaluated using,

$$\lambda_{tra} = \frac{15}{4} k_B \sum_{i \neq e} \frac{x_i}{\sum_r \alpha_{ir} x_i \Delta^2_{ir}} \tag{15}$$

and for the electrons,

$$\lambda_e = \frac{15}{4} k_B \frac{x_e}{\sum_r \alpha_{er} x_r \Delta^2_{er}} \tag{16}$$

in which,

$$\alpha_{ir} = 1 + \frac{[1 - M_i/M_r][0.45 - 2.54(M_i/M_r)]}{[1 - (M_i/M_r)]^2}$$

The global thermal conductivities for each internal mode (rotational, vibrational, and excitation), are calculated using

$$\lambda_{mode} = \sum_i \frac{x_i m_i C_{Vmode,i}}{\sum_r x_r \Delta^1_{ir}}, \quad mode \; = \; rot, \; vib, \; exc. \tag{17}$$

The multicomponent mass diffusion coefficient D_{ir} is given for each pair of species by,

$$D_{ir} = \frac{k_B T_c}{P \Delta^1_{ir}} \tag{18}$$

in which P is the total pressure of the gas. An average diffusion coefficient relative to the global remaining mixture can be obtained using,

$$D_i = \frac{1 - x_i}{\sum_{r \neq i} x_r / D_{ir}} \tag{19}$$

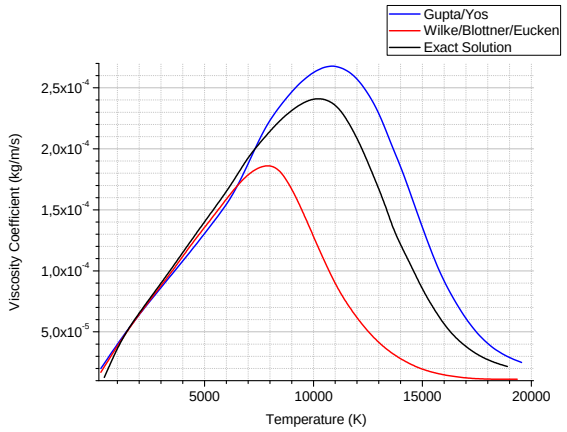

FIG. 1: Comparison between calculated viscosity coefficients using the Gupta/Yos model, the Wilke/Blottner/Eucken model, and the Chapman-Enskog solution [6].

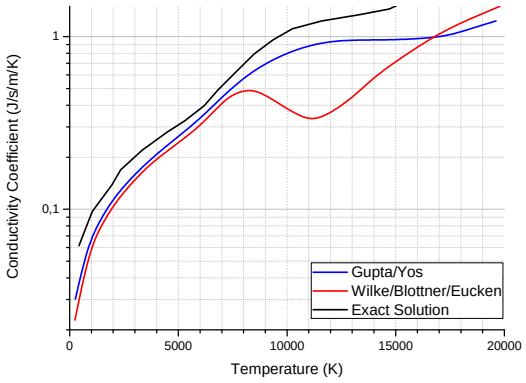

FIG. 2: Comparison between calculated conductivity coefficients using the Gupta/Yos model, the Wilke/Blottner/Eucken model, and the Chapman-Enskog solution [6].

This model is more accurate than the Wilke/Blottner/Eucken model, see Figure 1 and 2, [6] but it requires the knowledge of collisional integrals (see eq. 13), which may have not been measured for every pair of species being considered. Also, the collisional integrals provided by Gupta [14] are only accurate between 1000 K and 10000 K since the model was developed using data from [16]. The application of this model, using the collisional integrals provided by Gupta, is not suitable for cold APPJs. An expression is provided to calculate these collision integrals using differential-scattering cross sections [14],

$$\pi\bar{\Omega}^{l,s}_{i,j} = \frac{\int_0^\infty \int_0^\pi \exp(-\gamma^2)\gamma^{2s+3}(1-\cos^l\chi)4\pi\sigma_{ij}\sin\chi d\chi d\gamma}{\int_0^\infty \int_0^\pi \exp(-\gamma^2)\gamma^{2s+3}(1-\cos^l\chi)\sin\chi d\chi d\gamma} \tag{20}$$

in which $\sigma_{ij} = \sigma_{ij}(\chi, g)$ is the differential-scattering cross section for the species pair (i,j), χ is the scattering angle in the center-of-mass system, g is the relative velocity of the colliding particles and,

$$\gamma = g\sqrt{\frac{m_i m_j}{2(m_i+m_j)k_B T}}$$

is the reduced velocity. One should be able to calculate the necessary collision integrals by using other differential-scattering cross sections. However, Gupta uses the model developed by Yos, which uses the first aproximation of the Chapman-Enskog procedure [17]. A deeper literature review should be made to evaluate if the first approximation is valid at 300 K. Some other considerations of matters on numerical instabilities should be made [6]. Due to the low mass of electrons, there may be some problems in equations (13, 18, 19). Electron diffusion velocity can become very high, which can lead to nonphysical concentrations at the boundaries of the spatial domain. This in turn can cause unrealistic chemical non-equilibrium and may violate the quasi-neutrality assumption. In order to solve these problems, ambipolar diffusion should be included. This can be done by enforcing flux neutrality, and calculating electron mass diffusion fluxes trough the heavy species diffusion fluxes.

V. FINAL REMARKS

The correct calculation of multi-species transport is of great importance for non-equilibrium plasmas, as is the case of APPJs.

In a fluid model, the transport can be divided in advective and diffusive terms. Diffusive terms deal with transport due to microscopic interactions between species. Although an accurate description was provided by the Chapman-Enskog procedure, its computation is too expensive for the necessary real-time calculation of the coefficients. As a result, approximate models must be used.

The Wilke/Blottner/Eucken is simpler, requiring less input parameters, but with concerns about accuracy for high temperatures. The Gupta/Yos model is more accurate, see Figure 1 and 2, by considering the collisional cross sections between each pair of interacting species, but the necessary input parameters may not be available for every gas mixture. Also, the interactions strengths used in the Gupta/Yos model were calculate using collision integrals calculated for temperatures of $1000-10000$ K. These collision integrals should be calculated a at lower temperatures to properly simulate APPJs.

The inclusion of both these models should provide a solid framework for the calculation of transport coefficients in CFD simulations of APPJ.

Acknowledgements

This work was supported by Fundação para a Ciência e Tecnologia (grant PD/BD/142972/2018)

[1] G. Bauville, P. Jeanney, S. Pasquiers, and J. S. Sousa, "Propagation of a pulsed argon plasma jet in ambient air: importance of the gas flow," *Proceed. 9th International Workshop on Microplasmas*, 6-9 June 2017.

[2] X. Damany, S. Pasquiers, N. Blin-Simiand, G. Bauville, B. Bournonville, M. Fleury, P. Jeanney, and J. S. Sousa, "Impact of an atmospheric argon plasma jet on a dielectric surface and desorption of organic molecules," *Eur. Phys. J.: Appl. Phys.*, no. 75, p. 24713, 2016.

[3] K. Gazeli, G. Bauville, M. Fleury, P. Jeanney, O. Neveu, S. Pasquiers, and J. S. Sousa, "Effect of the gas flow rate on the spatiotemporal distribution of ar(1s5) absolute densities in a ns pulsed plasma jet impinging on a glass surface," *Plasma Sources Sci. Technol*, no. 27, p. 065003, 2018.

[4] T. Darny, J.-M. Pouvesle, V. Puech, C. Douat, S. Dozias, and E. Robert, "Analysis of conductive target influence in plasma jet experiments through helium metastable and electric field measurements," *Plasma Sources Sci. Technol.*, no. 26, p. 045008, 2017.

[5] J. P. Trelles, "Advances and challenges in computational fluid dynamics of atmospheric pressure plasmas," *Plasma Sources Sci. Technol.*, no. 27, p. 093001, 2018.

[6] D. D. Loureiro, "High-temperature modelling of transport properties in hypersonic flows," Master's thesis, Instituto Superior Técnico, 2015.

[7] S. Chapman, T. Cowling, D. Burnett, and C. Cercignani, *The Mathematical Theory of Non-uniform Gases: An Account of the Kinetic Theory of Viscosity, Thermal Conduction and Diffusion in Gases*. Cambridge Mathematical Library, Cambridge University Press, 1990.

[8] J. O. Hirschfelder, C. F. Curtiss, and R. B. Bird, *Molecular theory of gases and liquids*. New York: Wiley, 1954.

[9] R. B. Bird, W. E. Steward, and E. N. Lightfoot, *Transport phenomena*. New York: Wiley, 2002.

[10] C. R. Wilke, "A viscosity equation for gas mixtures," *The Journal of Chemical Physics*, vol. 18, p. 517, 1950.

[11] F. G. Blottner, M. Johnson, and M. Ellis, "Chemically reacting viscous flow program for multi-component gas mixtures," *Technical Report SC-RR-70-754*, 1971.

[12] G. E. Palmer and M. J. Wright, "A comparison of methods to compute high-temperature gas thermal conductivity," *36th AIAA Thermophysics Conference*, no. 1-16, pp. 2003–3913, 2003.

[13] L. C. Scalabrin, *Numerical simulation of weakly ionized hypersonic flow over reentry capsules*. PhD thesis, The University of Michigan, 2007.

[14] R. N. Gupta, J. M. Yos, R. A. Thompson, and K.-P. Lee, "A review of reaction rates and thermodynamic and transport properties for an 11-species air model for chemical and thermal nonequilibrium calculation to 30000k," *Technical Report RP 1232, NASA*, 1990.

[15] J. M. Yos, "Approximate equations for the viscosity and translational thermal conductivity of gas mixtures," *Technical Report, Contract Report AVSSD-0112-67-RM, Avco Corporation*, 1967.

[16] K. Yun, S. Weissman, and E. A. Mason, "High-temperature transport properties of dissociating nitrogen and dissociating oxygen," *The Physics of Fluids*, vol. 5, no. 6, pp. 672–678, 1962.

[17] J. M. Yos, "Transport properties of nitrogen, hydrogen, oxygen, and air to 30 0000 k," *Technical Memorandum, RAD-TM-63-7, Contract Report AF33(616)-7578, Avco Corporation*, 1963.

EAST spectroscopy calibration and experimental results on Mars entry

Ricardo was born in 1994 in Batalha, Portugal. He obtained is MSc degree in Engineering Physics at IST. In his thesis project he studied Laser ignition of H_2 combustible mixtures. First in the ESTHER prototype combustion chamber and later in collaboration with Clean Combustion Research Center at King Abdullah University of Science and Technology in Saudi Arabia. Plasma physics interest lead him into pursuing a research carreer starting with a PhD at APPLAuSE where he is part of the ESTHER team. During his free time Ricardo enjoys japanese anime and manga. As car and motorsport enthusiast he likes to learn more about the engineering behind racing cars. He hopes for one day to be part of a Formula One team.

Ricardo Ferreira

Instituto de Plasmas e Fusão Nuclear (IPFN), Instituto Superior Técnico
Avenida Rovisco Pais, 1049-001 Lisboa, Portugal
E-mail: `ricardojoaogmferreira@tecnico.ulisboa.pt`

Abstract. ESTHER is ESA's shock-tube currently being assembled at IST. Its main focus is to study kinetic processes of high enthalpy plasmas and help designing heat shields for planetary exploration. A summary of the NASA calibration method for the spectroscopy system of its shock-tube is presented. Test results for Mars atmosphere from the newest upgrade on NASA's EAST shock-tube are also presented. The tests ran from 0.01-0.1 torr at 6-8 km/s and 0.1-1 torr at 8-11 km/s for a composition of 96%-4% CO_2-N_2. The absolute radiance is resolved in both space and spectra and span from VUV to IR wavelengths. Dominant radiation was identified as being from CN violet and C_2 Swan bands.

I. INTRODUCTION

A new kinetic shock-tube ESTHER for the support of planetary exploration is currently being developed at Instituto Superior Técnico, under funding from the European Space Agency (ESA). This state-of-the-art facility, unique in Europe, will be used, for example, to design heat shields for spaceships, study the kinetic processes of high enthalpy plasmas, as well as others direct and indirect plasma physics topics. This kind of experimental facility, pioneer in Portugal, ushers a new age for Portuguese (and European) space research as result of increased performance.

As a spacecraft enters a planetary atmosphere its high-velocity results in the creation of a bow shock wave ahead of its blunt nose. The shock wave increases the gas temperature to tens of thousands of kelvin, leading to decomposition and ionization of the gas. The high gas enthalpy will cause a heat flux through the space vehicle, that requires the use of thermal protection systems (TPS). There are mainly two heating mechanisms in the planetary re-entry: convection where the energy is transferred to the heat shield via the gas flow, and radiation where excited gas molecules and atoms emit electromagnetic radiation, as they de-excite. The radiation will be absorbed by the TPS, heating its surface. The radiative flux is unimportant for low entry velocities (<8 km/s), yet it scales exponentially and becomes dominant for higher velocities (>12 km/s), as indicated in [1]. The radiative flux follows the relation $\rho R v^8$, where ρ is the gas density, R the nose radius and v the velocity, as cited in [2]. The radiative environment is unique to the gas composition, flow parameters, so it must be independently assessed for each individual scenario.

Since 2008, the Electric Arc Shock Tube (EAST) facility at NASA Ames is used to obtain validation data for radiative heating on planetary entry. The shock tube creates a sudden pressure discontinuity which will cause the formation of a shock wave. The shock wave moves hypersonically into the gas in front of it. Due to the short time scales, the pressure discontinuity compresses the gas in front rather than mix into it, similar to a spacecraft as it enters the atmosphere. The radiating shock is then imaged as it passes through the shock tube via a spectroscopy equipment. Data is collected simultaneous by four spectrometers covering from VUV to mid-wave infrared. Further details on the EAST facility are presented in [1]. In most cases of interest, a significant part (around 50%) of the emitted radiation is from the vacuum ultraviolet (100-200 nm) spectra. The remaining part comes from ultraviolet through near infrared (200-1200 nm), although in some cases mid-wave infrared (2000-6000 nm) can be dominant [1, 3]. ESTHER achieves a shock in similiar fashion.

This report focus on past experiments of EAST regarding Martian atmospheric entries to be in the future compared to the results from ESTHER. These tests will serve as a benchmark for ESTHER. Section II of the manuscript details the calibration method used in EAST, section III the main results from Tests 48 and 51, and it concludes in section IV.

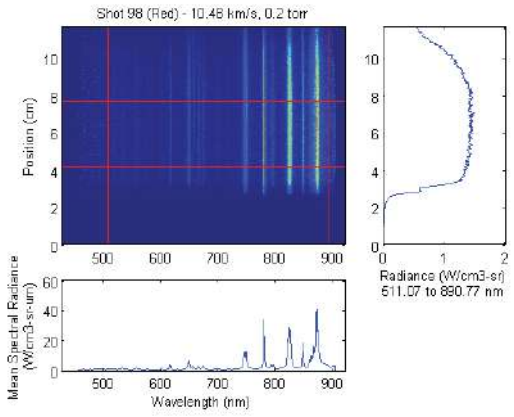

FIG. 1: Spectroscopy image example, from [1].

II. CALIBRATION

The spectroscopy equipment requires calibration in three quantities, corresponding to the x-, y-, and z-axis of the acquired images. Fig. 1 shows an example of a shock-tube spectroscopy image. The x-axis of the image corresponds to the wavelength, the y-axis to the time/spatial position and the z-axis (color scale) to the radiation intensity. Full details on the calibration method are presented in [1].

A. Spectral Calibration

The calibration in wavelength (x-component) is typically done using an "atomic line light source" such as mercury lamp for UV and visible light and the Lymann-α peak from a deuterium lamp for VUV. This type of light source has very defined emission wavelengths as one can observe, for a deuterium lamp, in Fig. 2. The collected data is then fitted to a numerical function, usually a second-order polynomial to obtained a relation between wavelength and horizontal pixels. The calibration is considered acceptable if the deviations between data and fitted function are smaller than two pixels. From the spectral calibration is also possible to estimate the instrument resolution function, or *instrument lineshape* (ILS). To measure ILS one assumes that the line source is infinitely thin and that all the broadening is due to the instrument. The ILS should be measured every time the spectrometer is altered in its focus, slit width, grating resolution or grating location. Typical ILS have been found to follow an empirical formula, with the form of a square root of a Voigt profile $[V(\Delta\lambda; \lambda_G; \lambda_L)]^{1/2}$. This profile is calculated by a convulsion of a gaussian G and

lorentzian L profiles. For a correct measurement of ILS the slit should be uniformly illuminated (i.e. overfilled), which may present a problem for larger slits.

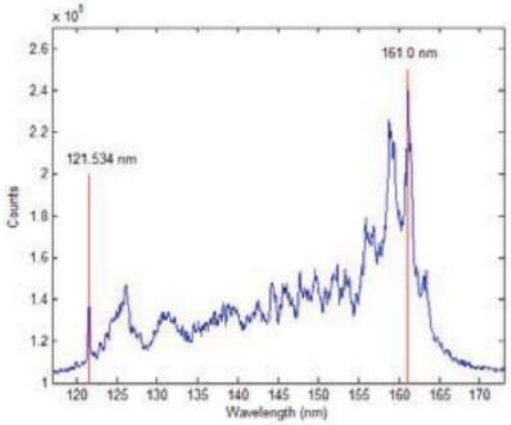

FIG. 2: Example of a spectral calibration image, deuterium lamp for VUV, in [1].

B. Spatial Calibration

Spatial (y-axis) calibration is done taking an image of a ruled object. A ruled transparent marker is placed in front of an illumination source at the focal plane. An image with distinct horizontal lines from the ruled marker is obtained, from which a linear relation distance/pixel can be derived. The y-axis can also be a temporal axis, to do so the spatial calibration must be divided by the shock wave velocity.

The resolution of the image in the y-direction is described by the *spatial resolution function* (SRF). It is a convolution of three main components, the optics' resolution, the CCD arrays' resolution and the shock wave motion during camera acquisition [1]. For a 10 km/s shock-wave a shutter of 1 μs corresponds to a movement of 1 cm in the camera. In a sub-μs regime the gating, shutter opening, and the gain, sensitivity of the pixels to light, cannot be approximated by a square wave as in long exposure times. Thus, they contribute for the spatial resolution of the camera. These can be measured with a pulsed light source faster than the gating function of the camera.

C. Radiance Calibration

The final calibration to perform is the radiance intensity calibration (z-component). The simplest way is to obtain the counts (camera units) for a known intensity radiation source. An integrating sphere is used to uniformly illuminate the camera. Some light scattering can occur inside the spectrometer, meaning that if the sphere

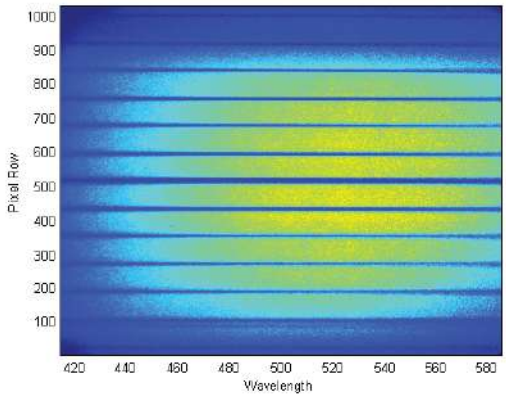

FIG. 3: Example of a spatial calibration image, each horizontal line distances 1 cm, in [1].

is smaller than the slit, adjacent areas of the slit may be polluted by scattered light. This scattered signal is known as pedestal, it is typical strong in UV and IR spectrometers. The pedestal often shows a wavelength dependence and needs to be corrected line by line. After this correction, the counts are divided by the instrument radiance calibration, usually provided by the manufacturer. The performed calibration is valid for the exposure time τ_c. However the experiment will be performed at a much shorter time τ_e. It is then needed to apply an exposure time correction. The intensity is most of the cases non-linear in relation to the exposure time [1]. This deviation is corrected by the use of a reciprocity factor r. To determine r one can either measure the gating function of the camera or measure the intensity for various exposure times and take the ratio of intensities. The collected data should be multiplied by $\tau_e r(\tau_c)/\tau_c r(\tau_e)$ to obtain the corrected intensity. Multiple images may be needed in the calibration to fully cover the image. These images are then stitched together to compose the response function.

III. EXPERIMENTAL CAMPAIGN

Here we summarize the reports of EAST experimental campaign on Mars entry experiments, both at high and low density, tests 48 and 51. The experimental data can be retrieved from NASA `website` [4].

A. Test 51

Test 51 was a set of experiments [3] performed to simulate high atmosphere entry on Mars. It was done to study the possibility of decelerate the vehicle in higher atmosphere than the traditionally for ballistic entry. At this altitudes, due to the lower gas density the gas takes longer to reach equilibrium after the shock. The experiment conditions are gas composition CO_2-N_2 (96%-4%),

shock wave velocity 6-8 km/s, pressure 0.05-0.25 torr. Data was obtained from both 4 and 24-inch diameter tubes. In Fig. 4 an example of the obtained data from the 4-inch tube is presented. The 3D image (center graphic) shows the volumetric spectral radiance as function of the wavelength (x-axis) and position (y-axis). The 2D plots correspond to the signal integration in position (bottom) or wavelength (right). From the 3D image it is observed that the shock starts around 3 cm and decays until 6 cm. The peaks at 359, 388 and 422 nm are characteristic of the CN violet transition, where the peak at 474 nm is of the C_2 Swan bands [5]. In Fig. 5 a comparison of

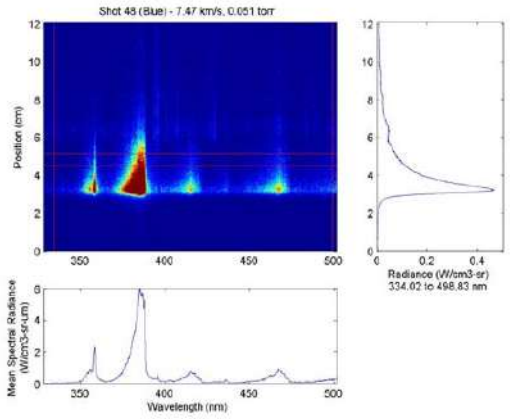

FIG. 4: Radiance behind the shock, in [3].

the spectral cross-section for three different conditions is shown. The shock velocity increases with lower pressures, as expected for an entry trajectory. For the red (6.8 km/s at 0.1 torr) and green (6.5 km/s at 0.25 torr) lines, the increased density is balanced with the reduced velocity so that the radiance is similar. The difference for the blue line integrated radiance (dashed line) is due to the VUV region. There the spectral radiance is higher, therefore the integrated radiance is higher. This VUV region is the CO fourth positive region. CN radiation magnitude is similar for all three test cases.

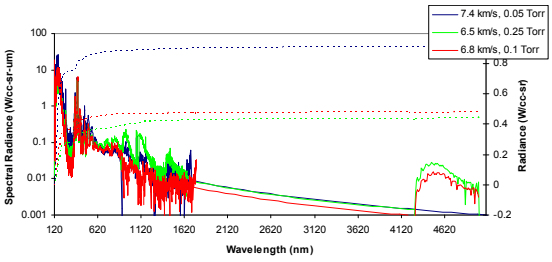

FIG. 5: Spectral cross-section after the shock, in [3].

During the test campaign, relaxation times for the chemical species and excitation modes were also studied. The times required for the rotational, vibrational, electronic and chemical parts to achieve a steady-state is presented in Table I. The relaxation times, in general, follow the ascending order of rotational, vibrational, electronic and chemical. The behaviour is expected as rotational and vibrational modes easily thermalize due to being a energy band closer to a continuum, than the electronic modes or the chemical reaction species. A plot of the radiance contribution for a shock at 0.1 torr and 6.8 km/s is shown in Fig. 6. The effect of optically thick and thin can be observed in the plot. The non-equilibrium radiation, right after the shock, is nearly dominated by the spectral region less than 170 nm, where the radiation is fully optically thick. This radiation is absorbed by the colder portions of the shock as the distance to the shock front increases. The region from 170-200 nm is partially optically thick in the non-equilibrium region, but becomes fully optically thick just beyond the shock front. Wavelengths larger than 200 nm remain optically thin for all the distance. This is evidenced by their linear dependence on position, shown in Fig. 6. Since the radiation with wavelengths larger than 200 nm is never absorbed by the gas it never decreases in intensity, thus its linear dependence with the position. The CN violet region from 340-500 nm is the strongest optically thin contributor. 40 cm beyond the shock front it becomes the dominant radiation. CN red contributions from 500-1600 nm, as well as the high wavelength tail of CO fourth Positive is also significant for the shock end.

TABLE I: Characteristic relaxation times in μs for low density Mars entry, from [3].

Condition	Rotational	Vibrational	Electronic	Chemical
0.05 torr 7.5-7.8 km/s	0.4-0.5	2.2-3.3	N/A	2.8-3.4
0.05 torr 7.1-7.3 km/s	0.9-1.2	2.6-4.8	2.8	7.4-9.0
0.1 torr 6.0-7.4 km/s	0.3-2.1	0.7-4.0	0.6-1.9	2.5-5.2
0.25 torr 6.3-6.8 km/s	0.3-0.4	0.3-1.0	0.5-1.2	1.7-1.8

B. Test 48

A series of shots, composing test 48, reproducing Venus and Mars entry conditions were reported in [2]. Both Mars and Venus gas compositions are of CO_2 and N_2. Venus has a 96.5% mass percentage of CO_2 where Mars is 96%. Mars tests were divided into 4 groups. The first, with pressure at 1 torr and velocity 7-8 km/s, focused on high-pressure conditions comparable to Venusian entries; second, pressure of 0.25 torr and velocity 6.8 km/s, to replicate the conditions of [6]; third, 0.1 torr at 8.5 km/s and 0.25 torr at 7.5 km/s to repeat the tests of [7]; and

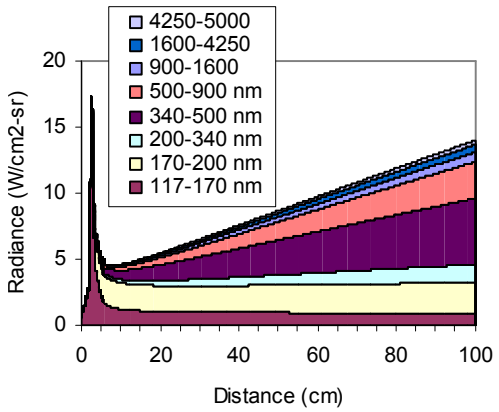

FIG. 6: Radiative heat spectra for a nominal condition of 0.1 torr and 6.8 km/s, in [3].

lastly, 0.2-1.0 torr at 3-4 km/s to study MWIR radiation of CO_2 vibrations.

Fig. 7 shows the radiance spectrum for six different conditions, both Martian and Venusian. From the spectra, one can observe that the radiation is strongly dependent on the velocity, as it increases two to three orders of magnitude from 6.5 to 11 km/s. A weaker pressure dependence is also observable as radiance increases from 0.1 to 1 torr, despite the drop in velocity from 8.5 to 7 km/s. A spectral dependence on the velocity is also reported. Below 10 km/s the dominant spectral region is 120 to 300 nm. It is mainly attributed to CO fourth positive system, peaking at 160 nm. Above 10 km/s this band gives place to continuum spectra at lower wavelengths. This radiation is associated with resonant states of the atoms N, O and C. The CN violet system (320-480 nm) is the seconds most important. The Planck curves plotted in Fig. 7 correspond to the radiation of a blackbody at post-shock equilibrium temperatures. Similar to the radiation, higher shock velocity will lead to higher temperatures, which correspond to higher radiation.

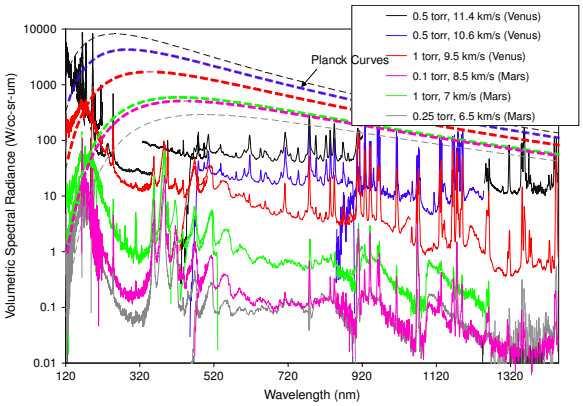

FIG. 7: Absolute radiance spectrum at six nominal conditions , in [2].

Fig. 8 presents the relative contributions of the different spectral regions for a shock at 0.5 torr at 11.5 km/s. The VUV region is clearly dominant over all the others. In contrast, the NIR (>900 nm) region contributes less than 12%. For slower shock-waves the VUV region is not so dominant as an increase in the IR region is presented. The results were also compared with the line-by-line ra-

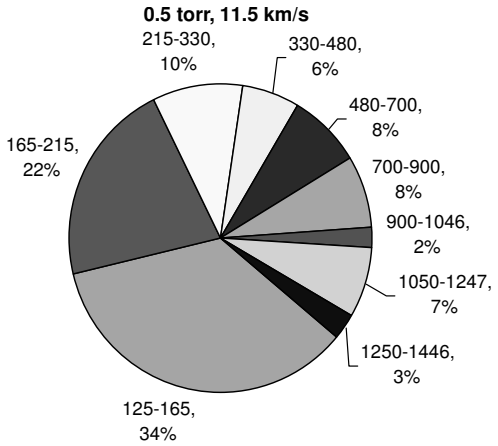

FIG. 8: Relative contributions of different spectral regions to the post-shock radiation, in [2].

diation code NEQAIR [2, 8]. It is reported that the code predicts well the CN and C_2 radiation, but presents major underpredictions with the continuum and CO fourth positive systems. This means that the total radiation is underpredicted by the numerical code.

IV. FINAL REMARKS

This report focused on summarizing the experimental research done on NASA shock-tube about Mars entry to be used as a comparison to the future ESA shock-tube. The calibration is a critical component of the spectroscopy and needs to be carefully addressed. It requires the use of "atomic source lines" for wavelength calibration and a rated known emission source for radiance calibration. Despite looking straightforward artifacts in the calibration can occur leading to inaccurate results and conclusions.

A couple of NASA test results on Mars entry were presented. The major radiative system is CO fourth positive in the VUV region. The radiation increases with the gas pressure and velocity. The velocity dependence is exponential. For low pressure entries a study on relaxation times was done and concluded that, in general, a steady-state is obtained in this order, first rotational, vibrational, electronic and finally chemical species.

[1] B. A. Cruden, "Absolute radiation measurements in earth and mars entry conditions," *NASA Reports*, 2014.
[2] B. A. Cruden, D. Prabhu, and R. Martinez, "Absolute radiation measurement in venus and mars entry conditions," *Journal of Spacecraft and Rockets*, vol. 49, pp. 1069–1079, nov 2012.
[3] B. Cruden, "Radiance measurement for low density mars entry," in *43rd AIAA Thermophysics Conference*, p. 2742, 2012.
[4] NASA, "Nasa website." `https://data.nasa.gov/docs/datasets/aerothermodynamics/EAST/index.html`, accessed february 2019.
[5] R. C. Johnson, "The structure and origin of the swan band spectrum of carbon," *Philosophical Transactions of the Royal Society A: Mathematical, Physical and Engineering Sciences*, vol. 226, pp. 157–230, jan 1927.
[6] H. S. Wright, D. Y. Oh, C. H. Westhelle, J. L. Fisher, R. E. Dyke, K. T. Edquist, J. L. Brown, H. L. Justh, and M. M. Munk, "Mars aerocapture systems study," 2006.
[7] J. H. Grinstead, M. J. Wright, D. W. Bogdanoff, and G. A. Allen, "Shock radiation measurements for mars aerocapture radiative heating analysis," *Journal of Thermophysics and Heat Transfer*, vol. 23, pp. 249–255, apr 2009.
[8] NASA, "Neqair website." `https://software.nasa.gov/software/ARC-15262-1B`, accessed february 2019.